nature communications

Article

https://doi.org/10.1038/s41467-026-74153-2

Regional, functional and transcriptomic decoding of multidimensional brain structure alterations in obsessive-compulsive disorder

Received: 27 December 2025

Accepted: 27 May 2026

Published online: 24 June 2026

Check for updates

A list of authors and their affiliations appears at the end of the paper

Studies of brain morphology in mental illness often focus on a few neuroimaging phenotypes. Here we present a comprehensive morphological characterization in obsessive-compulsive disorder (OCD) in a large sample (2255 OCD, 2264 controls) using nine cortical and four subcortical phenotypes, including several not previously examined in OCD, among them a subcortical structural similarity network phenotype developed here. Spatially distinct regional alterations emerged across structural phenotypes: cortical curvature alterations in default mode and frontoparietal networks, increased structural similarity network node degree in sensorimotor regions, widespread volume reductions associated with medication use, and localized subcortical shape alterations. In brain-behavior predictive models, curvature phenotypes showed the strongest associations with clinical features. Cortical alterations, especially in structural similarity networks, were associated with specific gene expression patterns, implicating dysregulation of excitatory neurons. RNA-sequencing data from tissue collected during functional neurosurgery revealed that genes downregulated in the dorsolateral prefrontal cortex in OCD contributed to the gene expression patterns linked to cortical alterations. Previously reported differentially expressed genes from postmortem brain studies of OCD also contributed. These findings support the importance of a comprehensive approach to characterizing brain morphology and suggest that cortical curvature and structural similarity alterations reflect key pathophysiological processes in OCD.

OCD was among the first mental disorders linked to specific regional brain alterations[1–3]. Four decades of neuroimaging research in OCD have fostered neurocircuit models of pathophysiology[4] and supported neurosurgical interventions in treatment-refractory cases[5,6]. Even so, OCD remains defined by subjective criteria, with no established neurobiological mechanisms or actionable biomarkers[7,8]. This persistent gap, even in a well-studied disorder, underscores the need for new strategies to probe neuroimaging data.

Human brain architecture is complex, and any of a large number of brain characteristics might be disrupted by pathology[9]. However, large-scale neuroimaging studies of OCD, and most studies in other mental disorders, have targeted only a few structural phenotypes—cortical thickness, cortical surface area, and regional volume—thereby capturing only a fraction of the complexity[10,11]. Modern genomics has advanced from single- to multi-omic approaches that integrate multiple biological layers to uncover underlying

e-mail: leonardo.saraiva@yale.edu; christopher.pittenger@yale.edu; carolina.cappi@rutgers.edu

mechanisms[12–14]. A similar shift toward multi-phenotype neuroimaging analysis could enhance our understanding of brain disruption by integrating complementary insights from phenotypes with distinct neurobiological underpinnings. For instance, curvature and sulcal morphology measures capture different aspects of cortical folding, which is critical to brain geometry and function[15]. Structural similarity networks leverage multiple phenotypes to estimate individual-level connectomes reflecting genetic, cytoarchitectonic, and anatomical coupling between brain regions[16].

Identifying robust neural correlates of mental disorders is challenging due to their substantial heterogeneity in genetic underpinnings, environmental influences, symptom constellations, and treatment exposures[17]. A normative modeling study found that although regional gray matter volume deviations are common in OCD patients, fewer than 5% of patients exhibit deviations in the same brain region[18]. To address this heterogeneity, emerging approaches derive patient subgroups (biotypes) directly from neuroimaging data. However, these data-driven clusters often struggle with reproducibility, and it is often unclear what drives subgroup boundaries, which could range from pre-existing vulnerabilities contributing to disease onset to post-onset exogenous factors that interact with and modify disease course[19,20]. A more interpretable alternative is to define subgroups based on participant characteristics, allowing differences in brain phenotypes to be attributed to observable rather than opaque latent factors. For example, medication use in OCD, which may be a marker of a more chronic or severe subtype, has been associated with more pronounced cortical thinning[10]. It remains unclear whether heterogeneity among patient subgroups manifests differently across multiple structural phenotypes.

In this study, we developed a multi-phenotype approach to comprehensively characterize brain morphology in OCD. Using the large, well-validated ENIGMA-OCD dataset ($n = 4519$), we assessed nine cortical and four subcortical structural phenotypes, including several not previously studied in OCD—and rarely in any mental disorders. As one of these, we developed a measure of structural similarity among subcortical regions to complement a recently established measure for cortical regions. These phenotypes revealed distinct patterns of regional alterations: cortical curvature, sulcal depth, and structural similarity networks showed more specific associations with OCD and aligned with distinct functional networks, while regional volume was broadly reduced only in medicated patients. Machine learning models identified curvature measures as top predictors of clinical characteristics. In addition, alterations in select cortical phenotypes—particularly structural similarity networks—exhibited a generalizable multivariate association with normative gene expression patterns, marked by pre- and postnatal excitatory neuron signatures. Finally, we performed a differential expression analysis of dorsolateral prefrontal cortex tissue collected during deep brain stimulation neurosurgery, revealing that downregulated genes significantly contributed to the transcriptional correlates of cortical alterations.

Together, these findings demonstrate that a comprehensive, multi-phenotype approach can advance the discovery of neural underpinnings of mental illness, supporting their adoption to better characterize mental disorders and behavioral traits more broadly.

Results

Sample and structural neuroimaging phenotypes

We analyzed data from 2255 OCD cases (age: 8–67 years; 1101 F and 1154 M) and 2264 neurotypical controls (age: 7–65 years; 1099 F and 1165 M) across 47 global datasets (Supplementary Fig. 1). Demographic, clinical, and scanner details are provided in Supplementary Tables 1, 2–7, and 8, respectively. For each participant, nine structural neuroimaging phenotypes were estimated for the 360 cortical regions defined by the HCP-MMP parcellation[21], including surface area, thickness, gray matter volume, Gaussian curvature, mean curvature, curvature index, folding index, and sulcal depth (Fig. 1). In addition, four neuroimaging phenotypes were estimated for seven bilateral subcortical regions—the thalamus, amygdala, caudate, putamen, nucleus accumbens, hippocampus, and globus pallidus—including volume, logarithm of the Jacobian determinant (reflecting surface deformation relative to a template), and radial distance (a proxy for cross-sectional dimension)[22–24].

In addition, we computed two structural similarity networks for each participant (Supplementary Fig. 2). The Morphometric INverse Divergence (MIND) network estimates pairwise similarity between cortical regions based on multivariate distributions of vertex-wise measures of surface area, thickness, volume, mean curvature, and sulcal depth (Methods)[25]. Given the relevance of subcortical structures in OCD, we developed a corresponding subcortical network, the subcortical MIND (scMIND), which applies the same approach using the logarithm of the Jacobian determinant (surface area) and radial distance to estimate structural similarity among subcortical regions. Both networks showed high inter-subject consistency (Supplementary Fig. 3) and robustness to threshold variation (Supplementary Fig. 4). For each network, node degree was calculated by averaging the non-thresholded edge weights between each region and all other regions, and this measure was used in all subsequent analyses, with any mention of MIND and scMIND hereafter referring to node degree.

Given evidence that medication use can affect structural neuroimaging phenotypes[10,11], we performed analyses on all OCD cases (OCD_{all}, $N = 2255$) and separately on subgroups with available medication information: unmedicated (OCD_{unmed}, $N = 1011$) and medicated (OCD_{med}, $N = 970$) cases, based on their medication status at scan time. Comparisons of clinical characteristics between OCD_{unmed} and OCD_{med} showed no significant differences in symptom severity, age of onset, or comorbid depression and anxiety (Supplementary Fig. 5). However, illness duration was longer in the OCD_{med} group (Welch's $t(816.17) = -7.60$, $p = 7.93 \times 10^{-14}$, Cohen's $d = 0.52$, 95% CI = 0.38 to 0.66).

Neuroimaging phenotypes capture distinct alteration patterns

We began by comparing regional neuroimaging phenotypes between OCD cases and controls. Harmonization of neuroimaging data across datasets was performed with NeuroCombat[26], and regional case–control differences were estimated using linear regression models adjusted for age, sex, Euler number (a scan quality index)[27], and total intracranial volume (Methods). Cohen's d values were estimated to quantify the effect sizes of group differences. Across all neuroimaging phenotypes, we found considerable variability in the patterns of alterations, both in regional distribution and in the magnitude and direction of effects (Fig. 2 and Supplementary Fig. 6).

Cortical surface area, thickness, and volume showed statistically significant alterations ($p\text{-value}_{FDR} < 0.05$), mostly reductions, dispersed across the cortex in OCD_{all}. The spatial patterns of these alterations differed considerably between OCD_{med} and OCD_{unmed}. OCD_{med} showed larger reductions spanning extensive frontal, parietal, and temporal regions in surface area, and affecting roughly one-third and one-half of regions in thickness and volume, respectively. In contrast, OCD_{unmed} exhibited smaller and less extensive alterations, with frontal involvement across phenotypes and scattered alterations elsewhere in the cortex. Overall, our findings largely align with prior large-scale studies showing more widespread reductions in these neuroimaging phenotypes only in medicated cases[10]. Cortical thickness reductions in OCD_{med} were similar in extent to prior findings, while alterations in surface area were previously described primarily in the parietal lobe but here extended into adjacent regions[10]. Previous work found no alterations in these measures in unmedicated patients, but we observed scattered alterations in OCD_{unmed}[10]. These subtle regional discrepancies may reflect the finer resolution of the HCP-MMP

https://doi.org/10.1038/s41467-026-74153-2

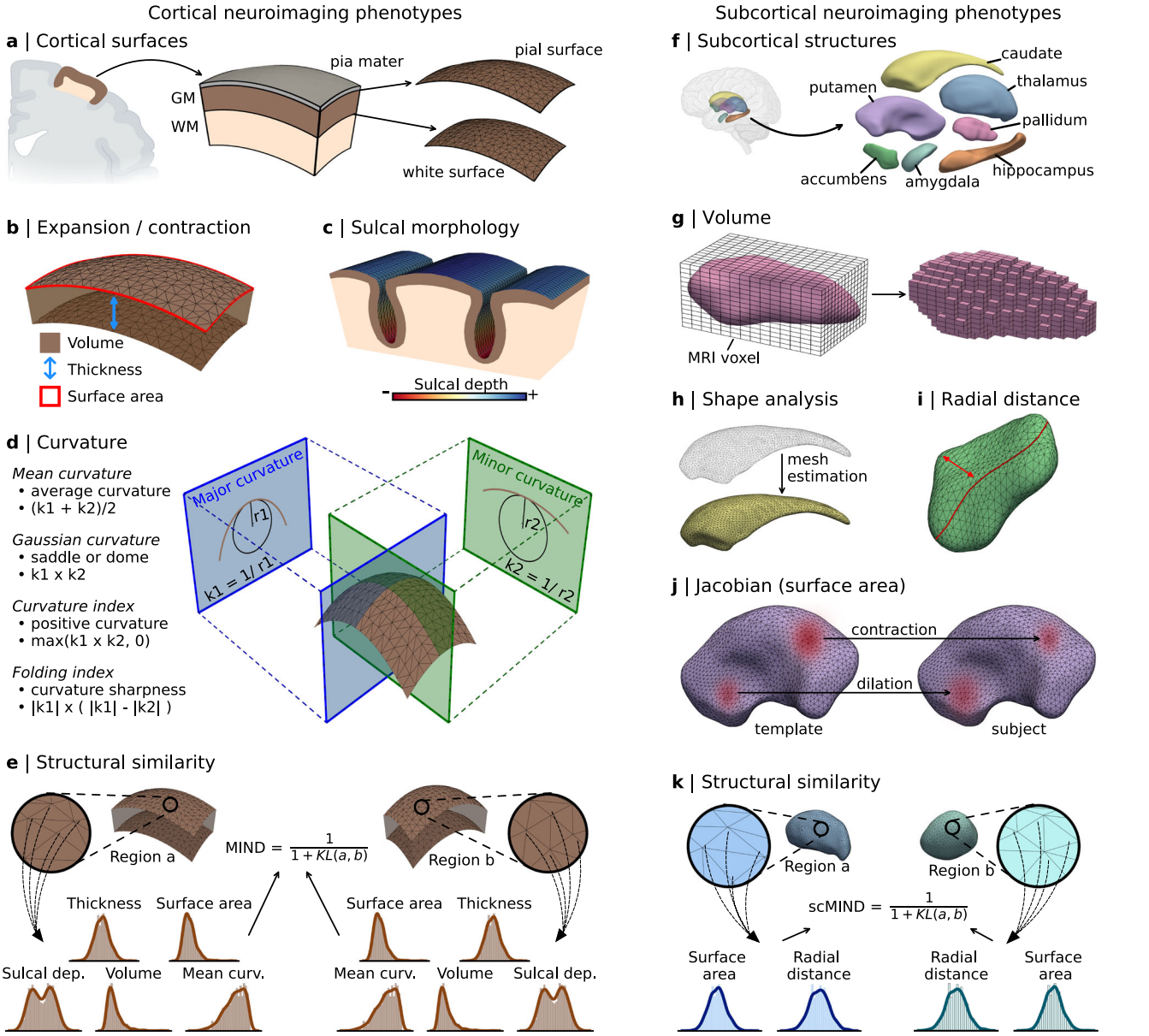

Fig. 1 | Cortical and subcortical neuroimaging phenotypes. a estimation of the pial and white surfaces using the automated recon-all pipeline from FreeSurfer; some elements of this panel were created in BioRender (Saraiva, L. (2026) https://BioRender.com/6fokbje). **b**–**d** cortical neuroimaging phenotypes estimated directly by recon-all: surface area, thickness, and volume (**b**), sulcal depth (**c**), and curvature measures (**d**). **e** cortical structural similarity estimated using the Morphometric INverse Divergence (MIND) network, derived from multivariate vertex-wise measures (thickness, surface area, volume, mean curvature, sulcal depth). **f** subcortical structures analyzed in this study; some elements of this panel were created in BioRender (Saraiva, L. (2026) https://BioRender.com/bnwqaux.). **g** subcortical volume estimated by voxel-wise segmentation, part of the default recon-all output. **h**–**j** surface meshes for subcortical structures estimated by the ENIGMA Shape analysis pipeline (**h**), enabling computation of vertex-wise radial distance (**i**) and logarithm of the Jacobian determinant (**j**). **k** structural similarity between subcortical structures, computed from vertex-wise measures obtained via the ENIGMA Shape pipeline using the same methodological approach as MIND; this subcortical measure is referred to as subcortical MIND (scMIND).

parcellation compared to the Desikan–Killiany parcellation previously used[10].

Cortical curvature, sulcal depth, and structural similarity each showed distinct patterns of significant alterations in OCD_{all}. Changes in curvature phenotypes primarily concentrated in frontal regions. Sulcal depth alterations spanned frontal, cingulate, and medial temporal cortices. MIND degree connectivity changes were seen in somatosensory and occipital regions. For these neuroimaging phenotypes, the affected regions were generally more similar across OCD_{unmed} and OCD_{med}. In OCD_{unmed} particularly, these phenotypes exhibited alterations comparable to or exceeding those observed in cortical surface area, thickness, and volume.

Subcortical alterations in surface area, radial distance, and volume showed similar sensitivity to medication status as their cortical counterparts (Fig. 2 and Supplementary Figs. 6–10). OCD_{med} exhibited widespread reductions in vertex-wise subcortical surface area and radial distance across regions, most prominently in the bilateral thalamus and hippocampus, while region-wise volume reductions were also observed in the bilateral caudate and amygdala and the right nucleus accumbens. The volumes of the hippocampus and nucleus accumbens have been shown to be affected in medicated adult and pediatric OCD cases, respectively, in a previous large-scale study[11]. In contrast to prior findings, volume alterations in the pallidum did not reach significance here. OCD_{unmed} showed more

https://doi.org/10.1038/s41467-026-74153-2

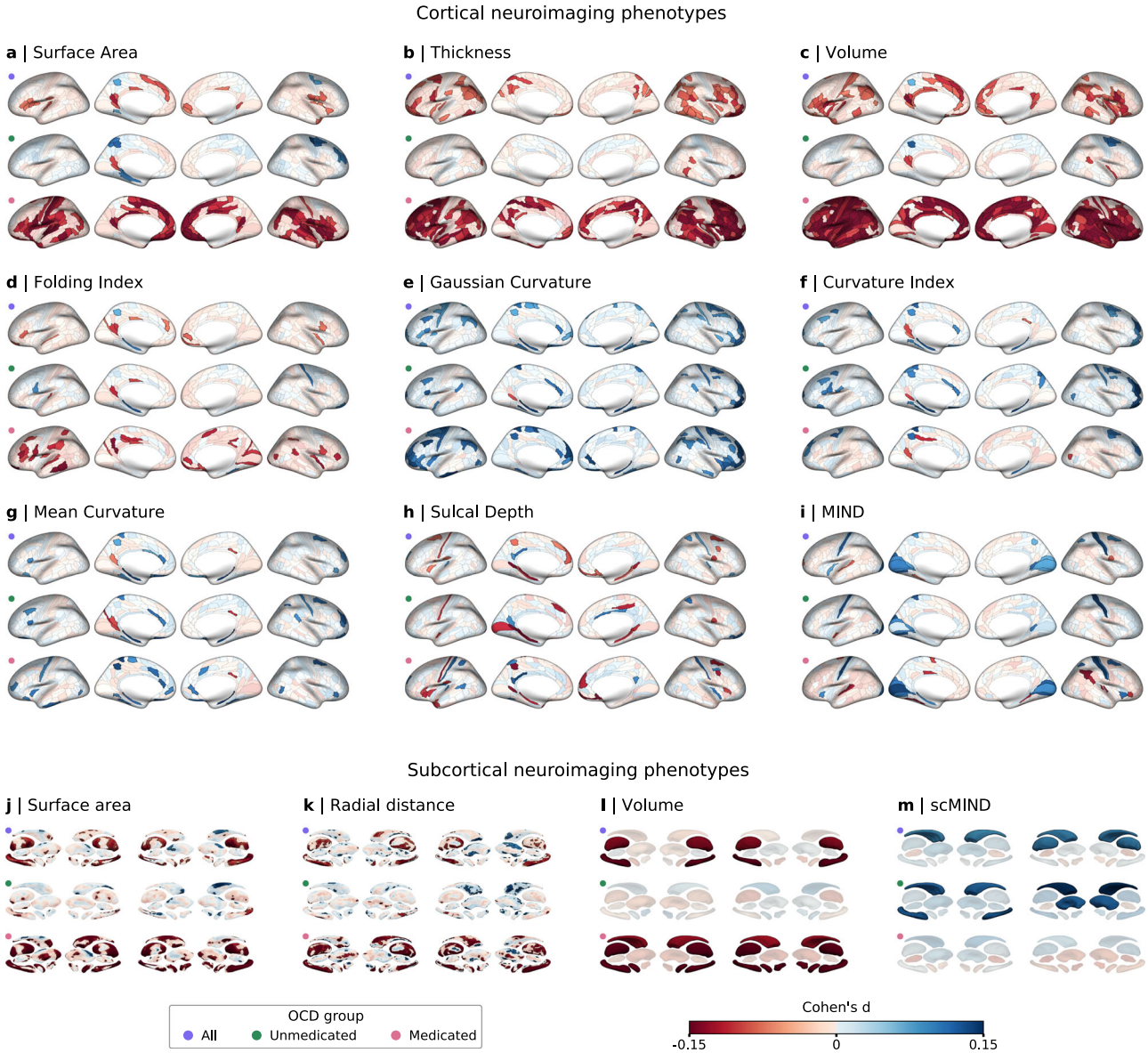

Fig. 2 | Regional alterations across cortical and subcortical neuroimaging phenotypes. a–i cortical surface maps showing effect sizes (Cohen's *d*) for case-control differences across regions defined by the HCP-MMP parcellation for nine neuroimaging phenotypes. In each panel, each row shows brain surfaces in the following views from left to right: left lateral, left medial, right medial, and right lateral. **j–m** subcortical surface maps showing effect sizes for case-control differences in seven subcortical structures—thalamus, amygdala, caudate, putamen, nucleus accumbens, hippocampus, and globus pallidus (Fig. 1f)—for four neuroimaging phenotypes. Each structure is shown from opposite viewpoints for each hemisphere (two left-hemisphere views on the left and two right-hemisphere views on the right). Vertex-wise analyses were conducted for (**j**, **k**) while region-wise analyses were conducted for (**l**, **m**). Cohen's *d* values were derived from linear regression models adjusted for age, sex, Euler number, and total intracranial volume. Separate models were fitted for OCD_{all} ($N = 2255$; top, purple), OCD_{unmed} ($N = 1011$; middle, green), and OCD_{med} ($N = 970$; bottom, pink), each compared against the same control group ($N = 2264$). *P*-values for regional case-control differences were adjusted using FDR for multiple comparisons across regions, neuroimaging phenotypes, and OCD groups. Positive Cohen's *d*-values (blue) indicate greater regional values in OCD cases relative to controls, while negative values (red) indicate a reduction. Statistically significant regions (or vertices) are emphasized with bold colors, while non-significant regions are muted. Source data are provided as a Source Data file.

limited changes—primarily an increase in vertex-wise measures in the right caudate—and no significant volume alterations. These vertex-wise changes in OCD_{unmed} were undetected in a previous study with a smaller sample[28], likely reflecting limited statistical power, whereas the absence of volume alterations aligns with previous adult findings[11].

scMIND node degree showed a different relationship to medication status. Significant increases in scMIND were observed in the bilateral caudate, right putamen, and left hippocampus in OCD_{unmed}, while no alterations survived FDR correction in OCD_{med}.

Similarity of regional alterations across neuroimaging phenotypes

We next asked to what extent the different neuroimaging phenotypes capture similar aspects of brain structure disruption in OCD. To examine this, we computed Pearson's correlation coefficients between the regional case-control differences (Cohen's *d*) across neuroimaging phenotypes and applied hierarchical clustering to group phenotypes with similar spatial patterns (Fig. 3a). The magnitude of these correlations could be influenced either by the intrinsic similarity of the neuroimaging phenotypes themselves (Supplementary Fig. 11)—such that high correlations may arise

https://doi.org/10.1038/s41467-026-74153-2

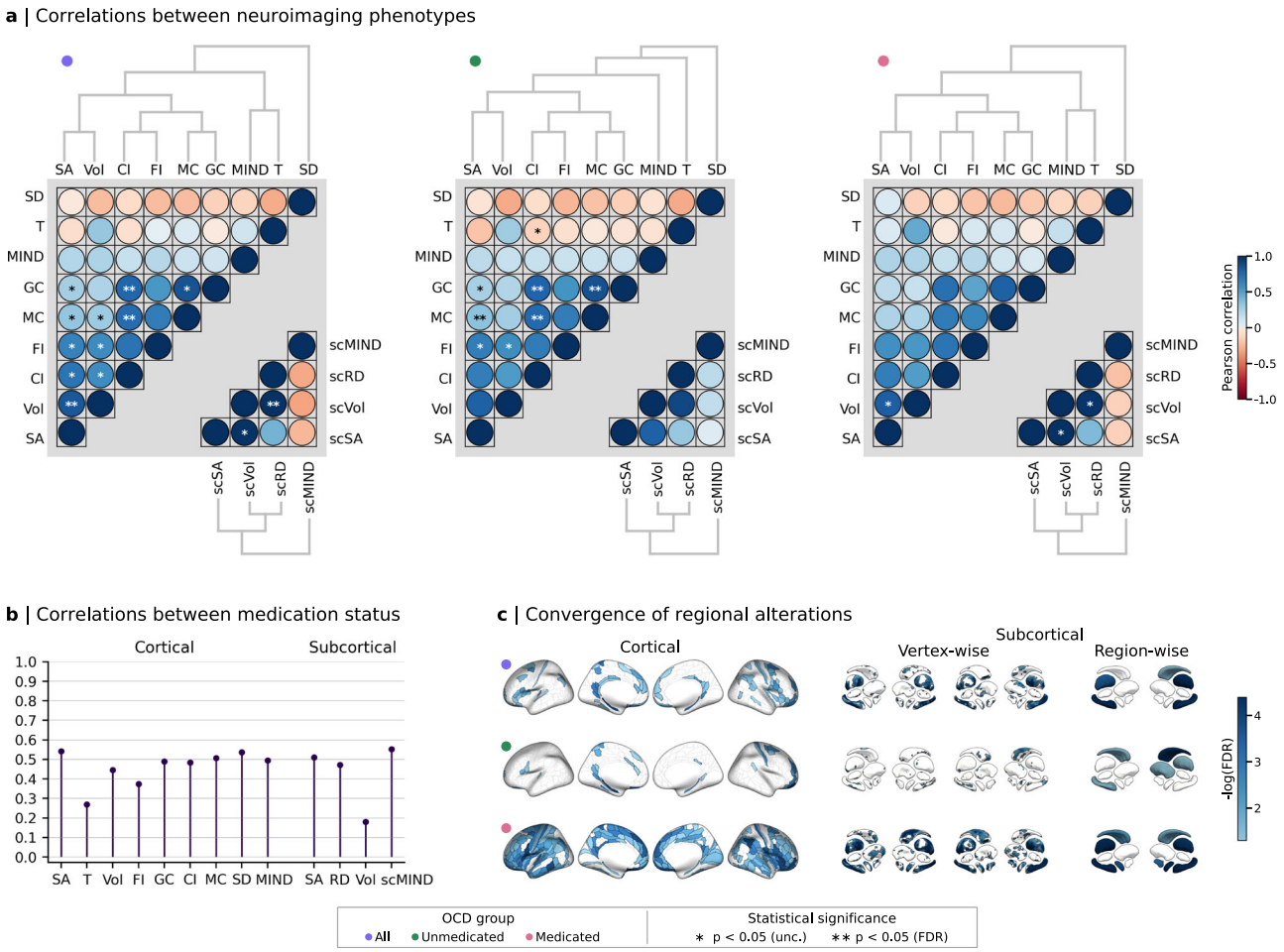

Fig. 3 | Similarity of regional alterations across neuroimaging phenotypes and medication status, and convergence of regional alterations across neuroimaging phenotypes. a heatmaps represent Pearson's correlation coefficients between regional Cohen's *d*-values for case-control differences (Fig. 2) across pairs of cortical and subcortical neuroimaging phenotypes. Correlations between subcortical surface area and radial distance were estimated vertex-wise, while correlations between subcortical volume and scMIND were computed region-wise. To estimate correlations between subcortical surface area (and radial distance) and subcortical volume (and scMIND), subcortical surface area (and radial distance) values were averaged across participants for each subcortical region. Statistical significance was assessed by comparing the observed absolute Pearson correlation coefficients with null distributions of absolute Pearson correlation coefficients generated by synchronous Freedman–Lane permutation of the regional linear models estimating case–control differences. *P*-values were FDR-adjusted across neuroimaging phenotypes and OCD groups. A double asterisk (**) corresponds to $p\text{-value}_{FDR} < 0.05$; a single asterisk (*) corresponds to $p\text{-value}_{uncorrected} < 0.05$. Dendrograms illustrate hierarchical clustering. Data are displayed for OCD_{all} (left, purple), OCD_{unmed} (middle, green), and OCD_{med} (right, pink). **b** Pearson's correlation coefficients were estimated between OCD_{unmed} and OCD_{med} case-control differences across regions for each neuroimaging phenotype. The stem plots display these correlations for cortical (left) and subcortical (right) neuroimaging phenotypes. **c** For each cortical region (left column), subcortical vertex (middle column), and subcortical region (right column), case–control differences were aggregated across all neuroimaging phenotypes using a non-parametric combination with Fisher's method. The statistical significance of the combined Fisher statistic was assessed using synchronized permutations of the underlying linear models. *P*-values were FDR-adjusted across regions, vertices, and OCD groups. Color encodes −log(FDR); only significant regions are shown. For the subcortical vertex-wise results, each structure is shown from opposite viewpoints for each hemisphere (two left-hemisphere views on the left and two right-hemisphere views on the right). Rows correspond to OCD_{all} (purple; top), OCD_{unmed} (green; middle), and OCD_{med} (pink; bottom). SA, Surface Area; T, Thickness; Vol, Volume; FI, Folding Index; GC, Gaussian Curvature; CI, Curvature Index; MC, Mean Curvature; SD, Sulcal Depth; scSA, subcortical Surface Area; scRD, subcortical Radial Distance; scVol, subcortical Volume. Source data are provided as a Source Data file.

between maps of group differences even when case-control labels are randomly assigned, simply due to the neuroimaging phenotypes being intrinsically related—or by similar patterns of brain structure disruption specifically reflected in the case-control differences across a pair of neuroimaging phenotypes, beyond what would be expected from the intrinsic similarity. To disentangle this, the statistical significance of the correlations was assessed via synchronous Freedman–Lane permutation of the linear models estimating regional differences, generating surrogate distributions of Cohen's *d*-values that were used to evaluate correlations under the null hypothesis of no case-control differences (Methods).

Following this procedure, few correlations among neuroimaging phenotypes achieved statistical significance, indicating that most correlations reflect intrinsic similarity among phenotypes. For the cortex, in both OCD_{all} and OCD_{unmed}, significant correlations were found mainly among curvature phenotypes, indicating that they capture spatially similar patterns of regional disruption in OCD beyond intrinsic phenotype similarity. For the subcortex, in OCD_{all}, the correlation of radial distance to volume was significant, whereas that of surface area to volume did not survive correction; in OCD_{med}, both were nominally significant, and in OCD_{unmed}, neither reached significance. In OCD_{med}, no correlations achieved statistical significance after FDR correction.

Similarity of regional alterations across medication status

We calculated Pearson's correlation coefficients between OCD_{unmed} and OCD_{med} regional case-control differences for each neuroimaging phenotype (Fig. 3b). Most correlations were moderate, with cortical thickness ($r = 0.27$) and subcortical volume ($r = 0.19$) showing the lowest similarity between OCD_{unmed} and OCD_{med}. These findings further demonstrate the marked effect of medication status on structural phenotypes, particularly commonly studied ones (cortical thickness and regional volume).

Convergence of regional alterations across neuroimaging phenotypes

We used a non-parametric combination to aggregate *p*-values for case-control differences across neuroimaging phenotypes within each region or vertex (Methods), assessing the extent to which alterations converged onto similar locations (Fig. 3c).

Cortically, in OCD_{unmed}, regional alterations converged predominantly onto the left frontal and somatosensory cortices, and onto scattered regions in the right frontal, parietal, and temporal cortices. In OCD_{all}, a similar but more extensive pattern was observed. In OCD_{med}, alterations converged across widespread regions.

Subcortically, vertex-wise alterations converged most extensively onto the right caudate in OCD_{unmed}, with additional clusters of alterations scattered throughout. More extensive convergence of alterations was observed in OCD_{all} and OCD_{med}, particularly in the bilateral hippocampus and thalamus. Region-wise subcortical alterations converged most pronouncedly in the right caudate in OCD_{unmed}, and in the bilateral thalamus and hippocampus in OCD_{all} and OCD_{med}.

Cortical and subcortical alterations across neurodevelopment

To evaluate how structural alterations in OCD manifest across different neurodevelopmental periods, we repeated the case-control analysis separately in pediatric (age < 18 years; 284 OCD cases and 251 controls) and adult (age ≥ 18 years; 1971 OCD cases and 2013 controls) subgroups. The results show different patterns of regional alterations for pediatric and adult patients (Supplementary Fig. 12), consistent with prior findings[10,11]. These differences may reflect the neurodevelopmental trajectory of OCD. However, this analysis is limited by its cross-sectional nature and by the relatively small pediatric sample. Future studies should aim to increase the pediatric sample size to better assess neurodevelopmental trajectories.

Robustness of regional alteration findings

To confirm the robustness of the structural alterations detected, we conducted several sensitivity analyses. First, as a validation of using medication status instead of other clinical variables in the stratified analyses, we re-estimated regional alterations using linear models that included two interaction terms: between diagnosis and medication status, and between diagnosis and each other available clinical variable (each included in turn alongside medication status), and compared the variance explained by each term. Across regions and neuroimaging phenotypes, the interaction between diagnosis and medication status generally explained more variance than the interaction between diagnosis and the other clinical variable; although, as expected, other clinical variables were more influential for some phenotypes and regions (Supplementary Figs. 13–17). Second, comparing regional alterations obtained using our NeuroCombat harmonization approach with those obtained using an alternative harmonization approach based on linear mixed-effects models revealed high agreement (Pearson's $r > 0.92$) across all neuroimaging phenotypes and OCD groups (Supplementary Figs. 18–20). Third, a leave-*k*-datasets-out analysis showed that once 20–30 datasets (approximately half of the total) were included, regional case–control effects remained highly correlated with full-sample effects (Pearson's $r > 0.8$) across all neuroimaging phenotypes and OCD groups, supporting the stability of our findings across different subsets of datasets (Supplementary Figs. 21–23).

Brain-behavior associations vary across neuroimaging phenotypes

We next used machine learning to examine the relationship of structural phenotypes to clinical features of OCD—severity, onset, illness duration, and comorbid anxiety and depression. Two modeling strategies were used: cross-region models predicting clinical features from each neuroimaging phenotype across regions; and cross-phenotype models predicting clinical features from each region across phenotypes. The statistical significance of model performance was assessed using permutation testing, with Freedman–Lane and Manly permutations for continuous and categorical clinical features, respectively ("Methods").

Predictive performance ranged from low to moderate, consistent with findings from other machine learning studies involving multi-site cohorts (Fig. 4). However, several models achieved statistically significant performance, suggesting generalizable associations between structural phenotypes and clinical characteristics. Several consistent patterns emerged.

In cross-region models, cortical curvature phenotypes consistently ranked among the best predictors, particularly for severity and onset in OCD_{unmed} and for depression and anxiety in OCD_{med}. Given that cortical curvature phenotypes remain underexplored in brain-behavior models, these findings highlight the informative value of less-studied neuroimaging measures. Additionally, stratifying participants by medication status generally improved model performance compared to analyses of the combined sample. This supports prior evidence that participant heterogeneity can impair brain-behavior models[29] and demonstrates that defining more homogeneous subgroups—rather than relying solely on broad diagnostic labels—enhances predictive accuracy. For example, severity and age of onset were generally predicted more accurately in OCD_{unmed}, whereas illness duration and comorbid depression and anxiety were generally better predicted in OCD_{med}.

Cross-region models using subcortical phenotypes showed relatively weak predictive performance overall. While some models achieved statistical significance, significant findings were sparse across OCD groups. This may reflect constraints of jointly modeling the examined subcortical phenotypes across all regions.

For cross-phenotype models, clinical characteristics were significantly predicted by only a few regions. This suggests that while measures from multiple brain regions are often needed for robust brain–behavior associations, combining multiple phenotypes within single regions can also reveal significant, localized relationships. For example, structural measures in somatomotor cortex regions were associated with symptom severity; parietal and frontal regions with illness duration; parietal regions with symptom onset; and frontal regions and the caudate with comorbid anxiety.

Taken together, these findings support expanding neuroimaging phenotypes and better delineating more homogeneous groups using broader participant characteristics to improve predictive performance of brain-behavioral models.

Structural alterations map to diverse functional networks

To explore the functional correlates of the different patterns of structural alterations identified (Fig. 2), we mapped them onto cortico-subcortical functional networks using the Cole-Anticevic atlas[30]. For each structural neuroimaging phenotype, we assessed the convergence of alterations within each network using a non-parametric combination approach[31]. This approach combines *p*-values for case–control differences from linear models across regions or vertices within a network, with statistical significance determined via synchronous Freedman–Lane permutations ("Methods").

https://doi.org/10.1038/s41467-026-74153-2

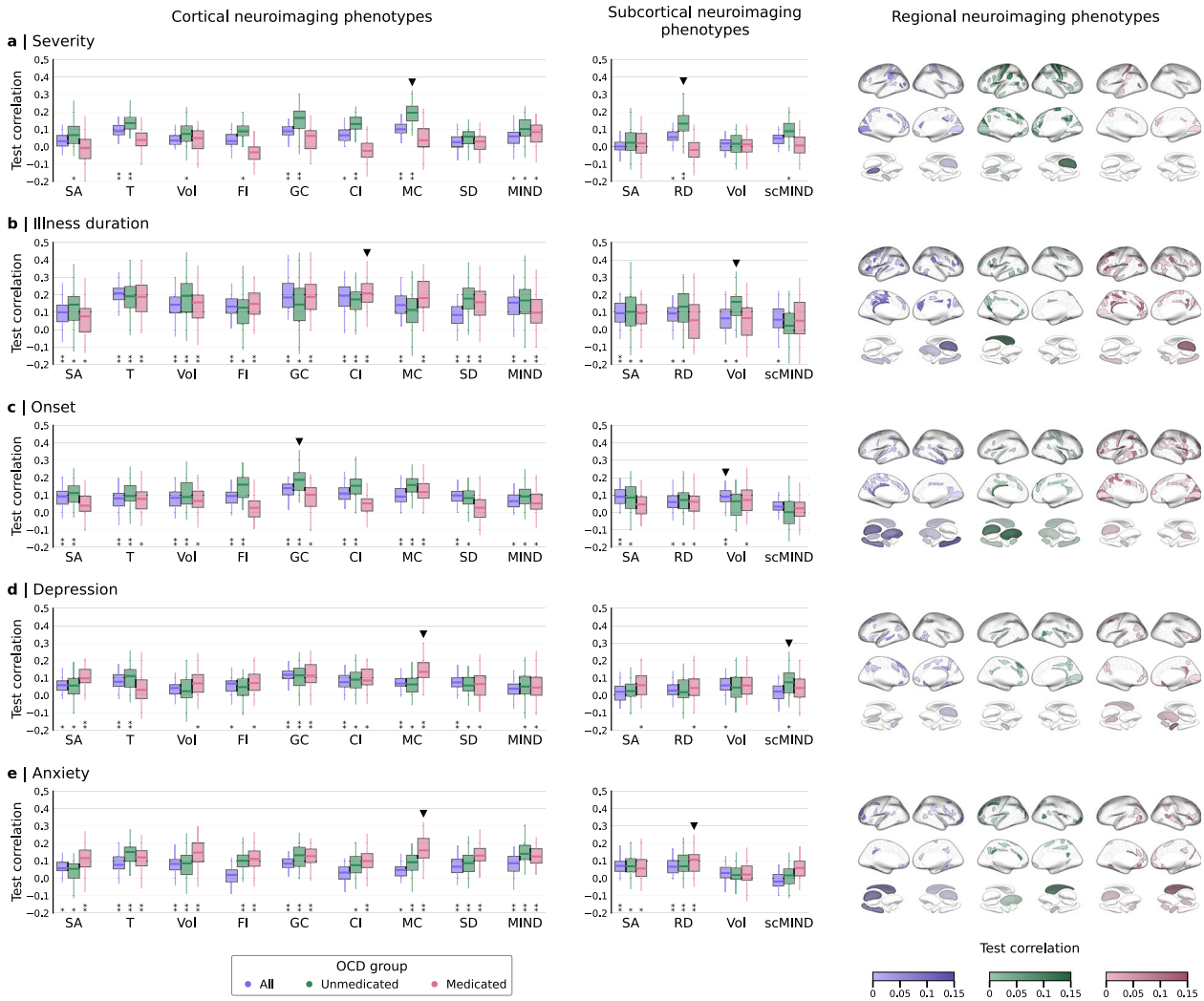

Fig. 4 | Brain-behavior associations between neuroimaging phenotypes and clinical characteristics of OCD. a symptom severity, measured with the adult or child Yale–Brown Obsessive–Compulsive Scale (N_{OCDall} = 2054, $N_{OCDunmed}$ = 982, N_{OCDmed} = 929); (**b**) illness duration in years since diagnosis (N_{OCDall} = *834*, $N_{OCDunmed}$ = 368, N_{OCDmed} = 457); (**c**) onset, early if before 18 years or late otherwise (N_{OCDall} = 1781, $N_{OCDunmed}$ = 908, N_{OCDmed} = 861); (**d**) current major depressive disorder (N_{OCDall} = 1901, $N_{OCDunmed}$ = 959, N_{OCDmed} = 852); and (**e**) current anxiety disorder (N_{OCDall} = 1897, $N_{OCDunmed}$ = 956, N_{OCDmed} = 851). Models were fitted in OCD cases and separately for OCD_{all} (purple), OCD_{unmed} (green), and OCD_{med} (pink). For continuous outcomes (**a**, **b**), ridge regression was used and performance measured with Pearson's *r*; for categorical outcomes (**c**–**e**), logistic ridge regression was used and performance measured with Matthews correlation coefficient (MCC). Model performance was assessed using a 5-fold, 10-times repeated nested cross-validation (50 outer folds). Statistical significance of model performance was assessed by permutation testing (Freedman–Lane method for continuous, Manly method for categorical outcomes), evaluating whether observed performance exceeded null distributions from permuted outcome variables. *P*-values were FDR-corrected across all models and OCD groups. Cross-region models (left and middle columns) are shown as box plots of model performance across 50 outer folds (center line, median; box bounds, 25th and 75th percentiles; whiskers, most extreme values within 1.5 × the interquartile range; outliers not shown). The arrows (▼) indicate the best-performing neuroimaging phenotype per panel. A double asterisk (**) corresponds to $p\text{-value}_{FDR} < 0.05$; a single asterisk (*) corresponds to $p\text{-value}_{uncorrected} < 0.05$. Cross-phenotype models (third column) are shown as brain maps of mean test performance across the same 50 outer folds; color scales represent Pearson's *r* (**a**, **b**) or MCC (**c**–**e**). Regions reaching FDR significance are bold; those reaching only nominal significance are muted. SA, Surface Area; T, Thickness; Vol, Volume; FI, Folding Index; GC, Gaussian Curvature; CI, Curvature Index; MC, Mean Curvature; SD, Sulcal Depth; scSA, subcortical Surface Area (log-Jacobian); scRD, subcortical Radial Distance; scVol, subcortical Volume. Source data are provided as a Source Data file.

As expected, regional case-control alterations of different neuroimaging phenotypes showed distinct functional network mappings (Fig. 5). For cortical surface area, thickness, and volume, medication status substantially influenced these mappings, with OCD_{med} showing significant ($p\text{-value}_{FDR} < 0.05$) alterations across most networks. This largely drove the functional mapping observed in OCD_{all}. By contrast, significant mapping of case-control differences was observed in only a few networks in OCD_{unmed}.

The other neuroimaging phenotypes showed greater consistency in functional mapping across medication status. Alterations in cortical curvature phenotypes and sulcal depth converged onto the default network across all OCD groups. Similar consistency was also observed for the orbito-affective, cingulo-opercular, and dorsal attention networks in Gaussian and mean curvatures, and for the frontoparietal and language networks in Gaussian curvature. These findings indicate that alterations in curvature and sulcal depth phenotypes align with functional networks classically implicated in OCD by resting-state and task-based functional MRI studies[32–38]. In addition, alterations in sulcal depth and MIND node degree aligned with the V1 visual and somatomotor networks across all OCD groups. This pattern matches emerging evidence that OCD involves disruptions in sensory networks[39].

https://doi.org/10.1038/s41467-026-74153-2

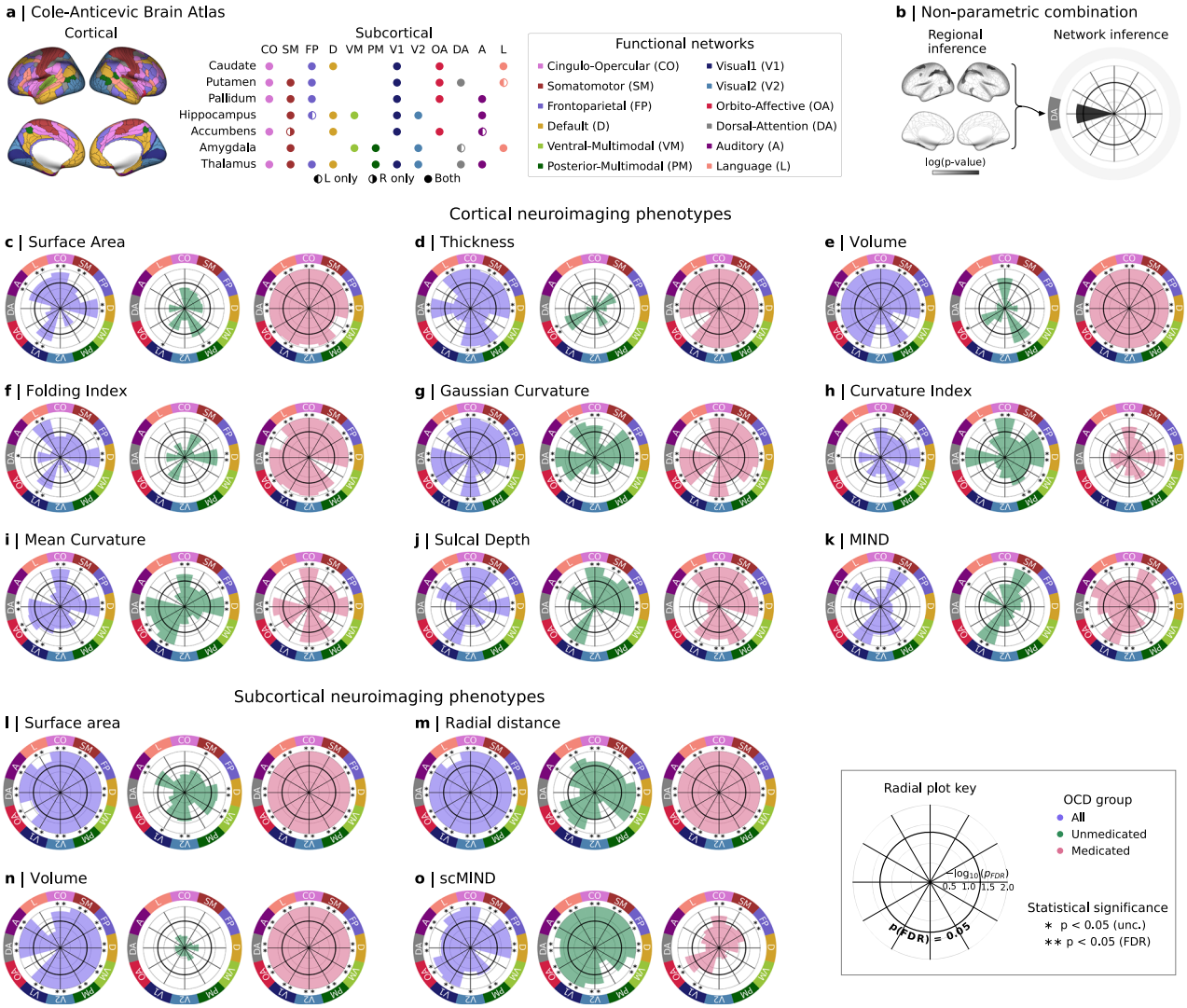

Fig. 5 | Functional correlates of case-control alterations across neuroimaging phenotypes. a schematic representation of the Cole-Anticevic atlas depicting its twelve functional networks. **b** schematic of the non-parametric combination approach for functional contextualization: *p*-values from regional linear models are aggregated across regions within each functional network using Fisher's method to yield a statistic reflecting evidence for case-control differences at the network level. The statistical significance of the Fisher statistic is assessed via synchronized Freedman–Lane permutations of the underlying linear models. The Dorsal Attention network is shown as an example, with regional significance, expressed as −log(*p*-values), shown on the cortical surface (color bar) on the left and the network-level Fisher-combined significance, expressed as −log(FDR), shown in the circular bar plot on the right. **c**–**o** for each cortical (**c**–**k**) and subcortical (**l**–**o**) neuroimaging phenotype, this approach was used to assess case-control differences (Fig. 2) at the network level. This analysis was performed separately for three OCD groups, each represented by a circular bar plot: OCD_{all} (left; purple), OCD_{unmed} (middle; green), and OCD_{med} (right; pink). Statistical significance was assessed as described in (**b**) with *p*-values adjusted for multiple comparisons using FDR across functional networks, neuroimaging phenotypes, and OCD groups. In each circular bar plot, functional networks are represented at each radial position, and the bars indicate network-level −log(FDR) values. A double asterisk (**) corresponds to $p\text{-value}_{FDR} < 0.05$; a single asterisk (*) corresponds to $p\text{-value}_{uncorrected} < 0.05$. The solid black line indicates −log(FDR) = 1.3 ($p\text{-value}_{FDR} = 0.05$). SM, Somatomotor; PM, Posterior-Multimodal; FP, Fronto-Parietal; CO, Cingulo-Opercular; L, Language; VM, Ventral-Multimodal; DA, Dorsal-Attention; OA, Orbito-Affective; V1, Visual 1; V2, Visual 2; D, Default; A, Auditory. Source data are provided as a Source Data file.

For subcortical neuroimaging phenotypes, volume abnormalities again aligned indiscriminately across functional networks in OCD_{med}, but showed no significant network convergence in OCD_{unmed}. While subcortical surface area showed significant convergence in fewer networks among OCD_{unmed}, subcortical radial distance and scMIND demonstrated more extensive network mapping across all OCD groups. This mapping particularly included the orbito-affective, frontoparietal, cingulo-opercular, and V1 networks, demonstrating consistent network-level alterations captured by both cortical and subcortical neuroimaging phenotypes.

Collectively, these findings highlight that different structural phenotypes provide complementary insights into the functional networks implicated in OCD.

Brain structure disruption correlates with gene expression patterns

To probe the neurobiological underpinnings of OCD, we linked structural alterations to normative gene expression patterns derived from the Allen Human Brain Atlas (AHBA)[40]. We used the rigorous quality control and preprocessing pipeline by Dear et al.[41], primarily validated for the HCP-MMP parcellation, to map the expression of 7973 genes to 137 left-hemisphere regions and derive three transcriptional components using diffusion map embedding (Fig. 6a). These components have been shown to be reproducible across donors and generalizable to other gene expression datasets[41]. We spatially associated these transcriptional components with brain maps of regional case-control differences in neuroimaging phenotypes, expressed as

https://doi.org/10.1038/s41467-026-74153-2

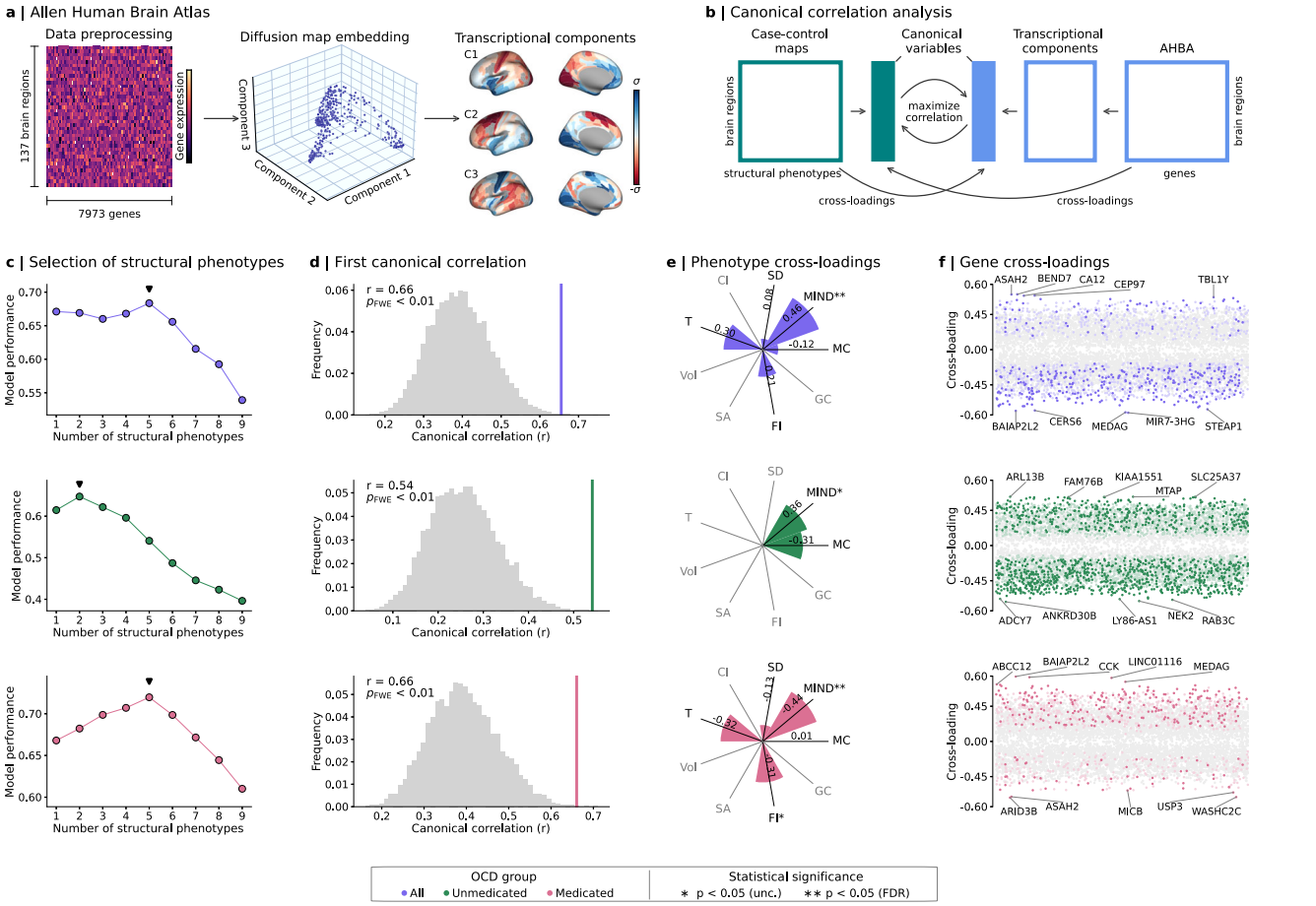

Fig. 6 | Spatial associations between brain structure alterations and gene expression. a procedure for obtaining generalizable gene expression components, as in Dear et al.[41]. **b** CCA methodology. **c** model performance in the split-half cross-validation procedure used to select neuroimaging phenotypes for association with the AHBA; performance was calculated as the average of two metrics: the average out-of-sample canonical correlation with the AHBA (model generalizability) and the average correlation of CCA weights across training folds (model stability). For each set size ($N = 1$ to $N = 9$ phenotypes), the plot shows the top-performing combination among all combinations of that size. The arrows (▼) indicate the overall top-performing combination. **d** the first canonical correlation using the whole sample between the case-control differences in the selected neuroimaging phenotypes (Fig. 2) and the AHBA. Statistical significance was assessed by permuting the regional linear models estimating case–control differences to generate surrogate case-control brain maps, from which null distributions for CCA were derived. *P*-values were corrected using the maximum statistic distribution within each OCD group, then Bonferroni-corrected across groups. Observed canonical correlations are shown as vertical bars against their null distributions. **e** radar plots of cross-loadings for neuroimaging phenotypes. Each radial axis shows absolute cross-loading magnitude, with signed values labeled. Double asterisk (**) indicates significance after FDR correction; single asterisk (*) indicates uncorrected significance. **f** plots showing cross-loadings for genes, with values shown on the *y*-axis; each point represents a gene: bold colors denote significance after FDR correction, muted colors uncorrected significance, and gray non-significance. The 5 genes with the most positive and 5 with the most negative cross-loadings are shown for each OCD group. For (**e**, **f**) statistical significance was assessed using the same permutation framework as in (**d**): surrogate case-control brain maps were used to generate null distributions for CCA and its cross-loadings, against which observed cross-loadings were evaluated by absolute magnitude. *P*-values were FDR-adjusted across all cross-loadings and OCD groups. SA, Surface Area; T, Thickness; Vol, Volume; FI, Folding Index; GC, Gaussian Curvature; CI, Curvature Index; MC, Mean Curvature; SD, Sulcal Depth. Source data are provided as a Source Data file.

Cohen's *d* from linear models (Fig. 2), using canonical correlation analysis (CCA) (Fig. 6b and Supplementary Fig. 24)[42]. This analysis proceeded in two sequential steps: first, feature selection to maximize model generalizability and stability; second, model fitting in the full sample with statistical significance testing (Methods).

In the first step (feature selection), we selected the neuroimaging phenotypes to include in the CCA models. With nine structural phenotypes, there are 511 (2^9–1) possible subsets for association with the AHBA. We exhaustively evaluated each subset for its ability to produce generalizable and stable CCA models linking brain structure disruption in OCD with gene expression, and selected the subset with the highest overall performance. To do this, we employed a split-half cross-validation approach: (i) split case-control data, (ii) derived maps of case-control alterations in each half, (iii) trained CCA on one half, and (iv) evaluated the first (maximal) out-of-sample canonical correlation on the other. Generalizability was defined as the mean out-of-sample correlation, stability as the mean correlation of CCA weights across folds, and overall performance as their average. Across all OCD groups, generalizability plateaued after including a certain number of case-control brain maps, whereas stability declined as additional maps were added (Supplementary Fig. 25). The optimal set for OCD_{all} and OCD_{med} included MIND degree, thickness, mean curvature, sulcal depth, and folding index (Fig. 6c). In contrast, OCD_{unmed} achieved best performance with only MIND degree and mean curvature (Fig. 6c), indicating these phenotypes are robustly linked to gene expression regardless of medication status.

In the second step (model fitting and significance testing), we computed CCA models using the optimal set of neuroimaging phenotypes on the full sample. To assess statistical significance, we used

synchronous Freedman–Lane permutations of the linear models estimating regional case-control differences to generate surrogate case-control brain maps that preserve spatial properties while removing group effects (Methods and Supplementary Fig. 24). These maps directly capture the null hypothesis, showing associations that would emerge without true case-control differences, while avoiding conventional spatial association significance tests, such as spin tests, that can inflate false positive rates[43,44]. Only the first canonical correlation was statistically significant across the CCA models for OCD_{all} ($r = 0.66$, $p\text{-value}_{FWE} = 0.009$), OCD_{unmed} ($r = 0.54$, $p\text{-value}_{FWE} = 0.0009$), and OCD_{med} ($r = 0.66$, $p\text{-value}_{FWE} = 0.003$) (Fig. 6d). This indicates that a single axis of association links brain structure disruption in OCD and gene expression across the neuroimaging phenotypes considered.

We next examined these associations at the level of individual case-control brain maps and genes. While all variables contribute to the associations identified by CCA, some may show stronger associations with the latent components of the opposite variable set than others. To quantify this, we calculated Pearson correlations between case-control brain maps and transcriptomic latent variables, as well as between individual gene expression maps and case-control latent variables; these correlations are referred to as cross-loadings[45]. To assess statistical significance, we evaluated cross-loadings against those computed from CCA models using the surrogate brain maps.

MIND showed the highest absolute cross-loading in OCD_{all} ($|r| = 0.46$, $p\text{-value}_{FDR} = 0.02$), OCD_{unmed} ($|r| = 0.36$, $p\text{-value}_{FDR} = 0.16$), and OCD_{med} ($|r| = 0.44$, $p\text{-value}_{FDR} = 0.02$) (Fig. 6e). It was the only imaging phenotype to achieve statistical significance in OCD_{all} and OCD_{med}; whereas the significance did not survive FDR correction in OCD_{unmed}.

In total, 365 genes showed statistically significant cross-loadings in OCD_{all}, 1221 in OCD_{unmed}, and 277 in OCD_{med} (Fig. 6f). Among these, 255 genes overlapped between OCD_{all} and OCD_{unmed}, 246 between OCD_{all} and OCD_{med}, 169 between OCD_{med} and OCD_{unmed}; of these, 165 genes were common across all three groups. To probe potential contributors to the differences in gene cross-loading significance patterns across OCD groups, we performed a leave-one-out analysis, re-running the CCA after excluding each case to assess their individual influence on each gene's cross-loading, defined as the relative change in its absolute value from the full-sample value. Individual influence was more variable in OCD_{med} (and consequently OCD_{all}) than in OCD_{unmed} (Supplementary Fig. 26), possibly reflecting greater heterogeneity from unmeasured clinical factors (e.g., treatment regimen, comorbidities) among medicated cases, which could introduce spatial structure into surrogate maps, broadening null distributions and reducing statistical power (Supplementary Fig. 27).

Probing the biological signatures of brain structure disruption

We next used enrichment analysis to assess whether specific cell types and previously reported genetic findings in OCD are represented in the brain-wide transcriptomic patterns underlying OCD-related structural alterations that were identified by our CCA models. Enrichment scores were computed as the average cross-loadings for genes within functionally defined gene sets. Statistical significance was assessed by recalculating enrichment scores using the surrogate brain maps, ensuring consistency with the null hypothesis used in the CCA (Methods).

We investigated enrichment for prenatal and postnatal cell types using data from psychENCODE I & II (Methods)[46,47]. For prenatal cell types, we observed significant enrichment for excitatory neurons in OCD_{all} and OCD_{unmed}; a similar enrichment in OCD_{med} did not remain significant after FDR correction (Fig. 7a). For postnatal cell types, there was significant enrichment for excitatory neurons across all OCD groups (Fig. 7b). These results implicate dysregulation of excitatory neurons in the structural brain disruptions observed in OCD.

Finally, we assessed the enrichment of genes previously implicated in OCD to gauge the concordance between our CCA analysis and established transcriptomic and genetic associations. First, we conducted a differential expression analysis of in vivo dorsolateral prefrontal cortex tissue collected during deep brain stimulation implantation surgery, using four samples from three OCD cases and six from four neurological controls ("Methods"). This analysis identified 478 upregulated and 153 downregulated genes in OCD cases ($p\text{-value}_{FDR} < 0.05$) (Fig. 7c). Down-regulated genes showed significant enrichment in the CCA models for OCD_{all}, OCD_{unmed}, and OCD_{med} (Fig. 7d).

Next, we assessed enrichment for previously reported up- and downregulated genes from postmortem differential expression studies in OCD (Piantadosi et al.[48] and Lisboa et al.[49]), and from the largest OCD genome-wide association study (GWAS) to date[50]. In the caudate, downregulated genes from both studies showed significant enrichment across OCD groups. In the nucleus accumbens, upregulated genes from Piantadosi et al. and downregulated genes from Lisboa et al. showed significant enrichment in OCD_{unmed}; upregulated genes from Lisboa et al. showed significant enrichment in OCD_{med}; and enrichment was not significant for OCD_{all} after FDR correction. In the putamen (Lisboa et al.), no significant enrichment was found in any group. Finally, GWAS-derived likely causal candidate genes showed nominally significant enrichment in OCD_{unmed}, though this did not survive FDR correction; no relationship was found in OCD_{med} or OCD_{all}.

Taken together, these results indicate substantial concordance between genetic findings in OCD and the transcriptomic associations identified by the CCA models.

Discussion

We show that cortical and subcortical morphological variation in OCD manifests differently across a range of neuroimaging phenotypes. Case-control differences in these phenotypes show distinct spatial distributions, functional signatures, and sensitivity to medication status, suggesting that they reflect different aspects of pathophysiology. A subset of phenotypes is robustly linked to spatial gene expression patterns reflecting differential-expression signatures of OCD. These findings support a shift toward comprehensive neuroimaging analyses that probe the complexity of brain morphology and its alterations in psychopathology.

Cortical surface area, thickness, and volume showed broad reductions in medicated cases, but only limited alterations in unmedicated cases (Fig. 2). This recapitulates previous findings in both OCD and other disorders[10,11]. Medication status appears to be a marker of a distinct patient subgroup whose more profound brain alterations could reflect clinical factors correlated with medication use, such as symptom severity, comorbidity, or duration of illness, in addition to medication use itself. Indeed, medicated patients had on average longer illness duration than unmedicated patients (Supplementary Fig. 5). Sensitivity analysis further indicated that, while medication status explained more variance than other clinical variables in cortical surface area, thickness, and volume, this pattern was not consistent across all regions (Supplementary Figs. 13–17). In addition, medication status masked putatively important diagnostic effects: functional contextualization of cortical thickness revealed convergence within the orbito-affective network, which is central to many models of OCD pathophysiology[32], only in unmedicated cases.

Subcortical surface area, radial distance, and volume also showed widespread reductions in medicated OCD cases (Fig. 2, Fig. 3c and Supplementary Figs. 7–10). No volume differences in whole structures were detected in unmedicated cases, consistent with prior studies[11]. However, in unmedicated cases, vertex-wise phenotypes revealed localized subcortical alterations. These were more extensive in the right caudate, with additional localized, often asymmetric, changes in other structures. Considering the well-established subcortical

https://doi.org/10.1038/s41467-026-74153-2

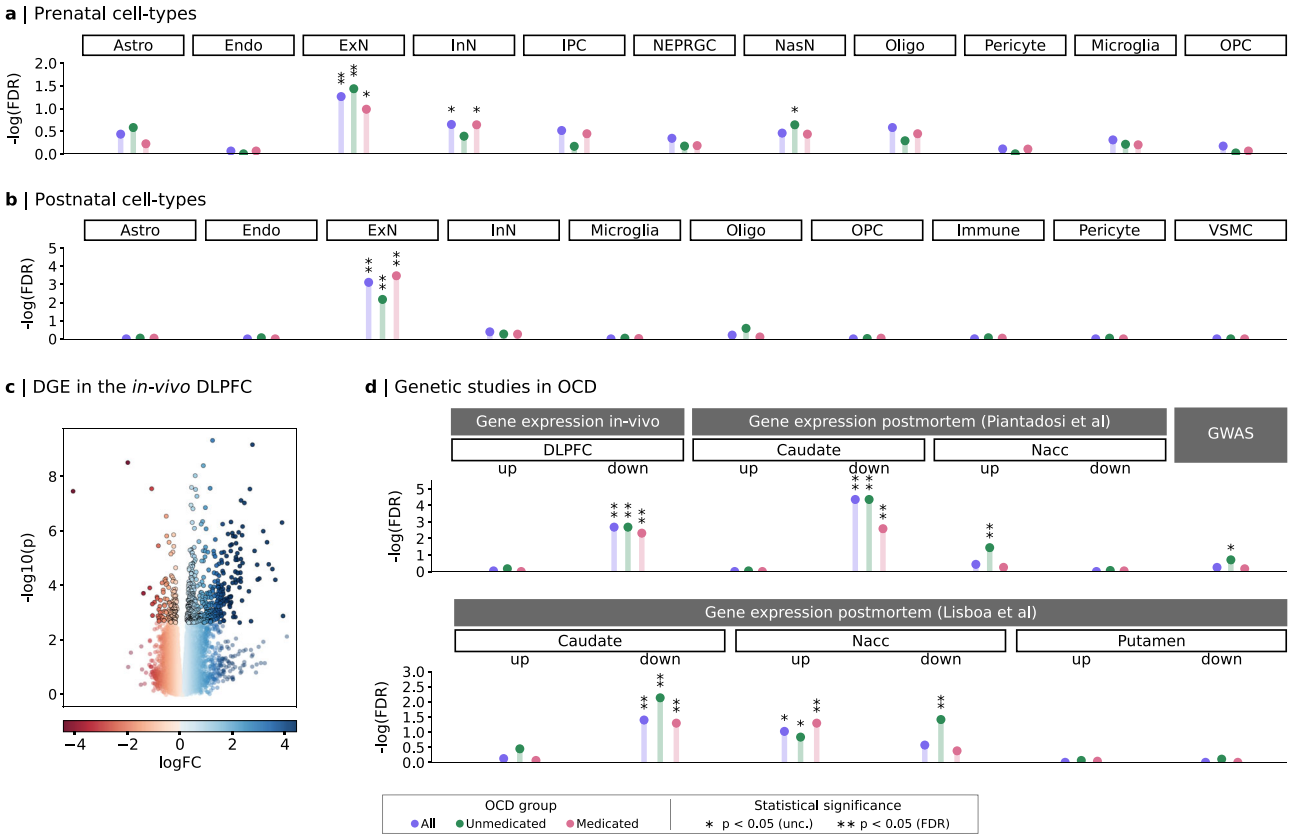

Fig. 7 | Enrichment analyses for cell-type signatures across neurodevelopment and OCD-related differential expression. a, **b** stem plots showing enrichment analysis for gene sets derived from prenatal (**a**) and postnatal (**b**) cell-type expression profiles. **c** volcano plot illustrating genes differentially expressed in OCD identified in dorsolateral prefrontal cortex tissue obtained during deep brain stimulation neurosurgery, with 4 samples from 3 OCD cases and 6 samples from 4 neurological controls. Differential gene expression (DGE) was assessed using linear mixed-effects models with empirical Bayes moderation, adjusted for age, sex, RIN, and one surrogate variable, with subject as a random effect. The *x*-axis shows $\log_2$ fold change (logFC). *P*-values for differential expression were FDR-corrected for multiple comparisons across genes. Genes significantly upregulated or downregulated after FDR correction are displayed in brighter colors, while the remaining genes appear muted. **d** stem plot depicting enrichment analysis for gene sets comprising differentially expressed genes from intraoperative dorsolateral prefrontal cortex tissue in OCD, differentially expressed genes reported in prior postmortem studies[48,49], and causal candidate genes from a recent GWAS[50]. Across all enrichment analyses (**a**, **b**, **d**), statistical significance was assessed within the CCA inference framework: regional linear models estimating case–control effects were synchronously permuted to generate surrogate case-control brain maps, from which null distributions of CCA-derived enrichment scores were computed. Observed enrichment scores were then compared against these null distributions by absolute magnitude. *P*-values were adjusted for multiple comparisons using FDR across gene sets and OCD groups. In stem plots, bars represent −log(FDR) values for each gene set. A double asterisk (**) corresponds to $p\text{-value}_{FDR} < 0.05$; a single asterisk (*) corresponds to $p\text{-value}_{uncorrected} < 0.05$. Results are shown for OCD_{all} (purple), OCD_{unmed} (green), and OCD_{med} (pink). Astro, astrocyte; Endo, endothelial cell; ExN, excitatory neuron; InN, inhibitory neuron; IPC, intermediate progenitor cell; NEPRGC, non-epithelial progenitor radial glial cell; NasN, nascent neuron; Oligo, oligodendrocyte; Pericyte, pericyte; Microglia, microglial cell; OPC, oligodendrocyte progenitor cell; Immune, immune cell; VSMC, vascular smooth muscle cell. Source data are provided as a Source Data file.

involvement in OCD[4,7], these findings suggest that it may localize to the subregional rather than whole-structure level.

Four curvature measures and sulcal depth, structural phenotypes not previously examined in OCD, were used to assess cortical folding. Folding is an evolutionarily conserved strategy for accommodating an expanded cortex within the skull while minimizing wiring and optimizing the clustering of interconnected regions[51,52]. It emerges from tightly regulated genetic programs interacting with biomechanical forces and environmental cues, producing stereotyped gyral–sulcal patterns that can predict cytoarchitectonic boundaries, such as Brodmann areas, with millimeter accuracy[53]. Cortical folding has been investigated in psychiatric disorders, but most studies have had moderate sample sizes, with early findings in schizophrenia, autism, and major depression suggesting that subtle alterations may contribute to pathophysiology[54]. Our large-scale study identified localized curvature and sulcal depth abnormalities in OCD (Fig. 2); of note, these effects were less affected by medication status, suggesting that they relate to core OCD processes. Functional mapping showed that these alterations converged on canonical OCD networks: the default mode, whose overactive self-referential processing fuels intrusive thoughts; frontoparietal, where reduced top-down control impairs cognitive flexibility; orbito-affective, where altered valuation biases threat and error appraisal; cingulo-opercular, whose heightened performance monitoring sustains not-just-right experiences; and dorsal attention, where impaired external reorienting traps cognition in internal loops (Fig. 5)[32–38]. Since cortical folding develops prenatally and in early infancy and remains relatively stable thereafter[51,52,55], the mapping of folding alterations onto these networks suggests their dysfunction in OCD may have neurodevelopmental origins. This aligns with genetic and epidemiological evidence implicating abnormal neurodevelopment in OCD[56,57]. However, the cross-sectional nature of this study precludes definitive conclusions as to when these alterations emerged, which warrants investigation in future studies.

Structural similarity networks quantify morphological similarity between brain regions by integrating multiple MRI features into single-

subject connectomes[16]. Among these, the MIND network is well validated, aligning with cortical cytoarchitecture, gene co-expression, and tract-tracing measures of axonal connectivity[16]. Moreover, node degree in structural similarity networks has been shown to predict age[16] and intelligence[58] and is disrupted in conditions such as schizophrenia[59], major depression[60], and chromosomal disorders[61]. Here, we applied MIND to OCD. The original MIND network excludes the subcortex; we overcame this by developing the scMIND network, which incorporates vertex-wise measures from the ENIGMA shape analysis pipeline. In both unmedicated and medicated cases, MIND and scMIND node degree showed localized increases (Fig. 2) that functionally mapped to sensorimotor networks (Fig. 5). Although historically under-explored in OCD, sensorimotor dysfunction relates to core clinical phenomena: aversive sensory experiences and dominance of habits over goal-directed control. Indeed, the largest OCD resting-state mega-analysis reported pervasive global hypoconnectivity that was most pronounced within the sensorimotor network[39]. Because MIND and scMIND index inter-regional similarity, elevated node degree indicates that a region is less differentiated from the rest of the cortex. Recent work shows modest and developmentally decreasing coupling between structural similarity and functional connectivity. This has been interpreted as indicating that maturation yields greater structural differentiation (i.e., lower structural similarity) alongside stronger functional interactions over the course of development[62]. The increased structural similarity (reduced differentiation) of the sensorimotor cortex in OCD may reflect atypical maturation that contributes to functional dysconnectivity, which may impair functions normally supported by mature sensorimotor cortices, such as the modulation of aversive sensory experiences and of habit formation.

We examined brain-behavior associations between neuroimaging phenotypes and clinical characteristics of OCD using predictive models (Fig. 4). We constructed two categories of models: cross-region models, in which the predictors were each structural phenotype across regions; and cross-phenotype models, in which the predictors were each brain region across structural phenotypes. In cortical cross-region models, the best-performing neuroimaging phenotypes varied across clinical characteristics; however, cortical curvature phenotypes consistently ranked among them, suggesting that folding captures clinically relevant variance in OCD. Prior studies have shown that gyrification alterations are related to age of onset in OCD[63], and our findings extend this by suggesting that folding may relate to clinical features in addition to symptom onset. Cortical cross-phenotype models revealed a range of regional mappings to clinical characteristics. Symptom severity mapped primarily to sensorimotor cortices and additionally to distributed cortical regions, particularly in unmedicated patients. This distributed pattern may reflect our use of aggregate severity scores; prior studies using dimension-specific scores found more localized mappings that varied by dimension but generally overlapped with those observed here[64]. Illness duration mapped mainly to frontal, parietal, and cingulate cortices, especially in medicated patients, partially aligning with regions whose node centrality correlated with illness duration in a large-scale structural covariance study of OCD[65]. Depression comorbidity mapped to relatively few regions, while anxiety comorbidity mapped more consistently to frontal areas, a pattern not observed in prior large-scale structural studies of anxiety[66]. This may reflect a distinct signature of anxiety comorbidity in the context of OCD, though this divergence may also reflect differences in analytic approach or differing definitions of anxiety between this and prior studies.

Cross-region models were largely non-significant for subcortical structures, whereas several individual regions reached significance in cross-phenotype models; in the cortex, both cross-region and cross-phenotype approaches yielded significant predictions. This discrepancy may reflect distributed, directionally consistent cortical effects that ridge regression leverages effectively across regions, contrasted with more focal, directionally inconsistent subcortical effects that are diluted when modeled jointly across structures but preserved in structure-specific models. In subcortical cross-phenotype models, thalamus, caudate, putamen, and hippocampus most prominently predicted clinical characteristics, with many associations found only in one hemisphere. This is consistent with their roles in distinct aspects of OCD: the thalamus in cortico-striato-thalamo-cortical loops implicated in compulsivity, the caudate and putamen in frontostriatal gating and habit formation, and the hippocampus in contextual memory and fear[4,67,68]. The observed lateralization aligns with prior asymmetry findings in OCD[69].

We used CCA to link structural brain alterations in OCD to normative gene expression patterns (Fig. 6). Since brain structure and OCD are heritable and genetically associated through pleiotropic variants[56,67,70], this analysis assessed whether their association also has transcriptional underpinnings. To ensure robust associations, we used split-half cross-validation to identify neuroimaging phenotypes with generalizable and stable associations to AHBA-derived transcriptional components. MIND node degree and mean curvature were consistently selected regardless of medication status, suggesting they capture fundamental links between structural brain alterations in OCD and gene expression. This is consistent with evidence that structural similarity tracks inter-areal gene co-expression and that cortical folding is genetically regulated[16,51]. Using these phenotypes, we fit CCA in the full sample and applied the well-validated Freedman–Lane permutation procedure[71,72] adapted for spatial association testing. This revealed a single significant multivariate axis linking structural alterations in OCD to gene expression, indicating a transcriptional substrate for these alterations.

We next assessed variable-level associations using cross-loadings, the correlations between each variable and the opposite-side canonical variable. Cross-loadings indicate which variables exhibit salient associations beyond their contribution to the multivariate CCA combination. In unmedicated cases, MIND node degree showed a slightly larger cross-loading than mean curvature and reached nominal significance. In addition, many genes showed significant cross-loadings, indicating a broad and distributed transcriptional signature underlying structural alterations. Conversely, the CCA models for medicated patients and for all patients exhibited different cross-loading statistical significance patterns. Medication status altered the correlation structure of regional case–control differences among neuroimaging phenotypes (Fig. 3a), which may have similarly shifted their correlations with the gene-expression canonical variable, amplifying cross-loadings with MIND. At the individual level, medicated cases may be more clinically heterogeneous in ways not captured by available data (e.g., treatment regimens). In spatial association testing, even attenuated effects from unmodeled variability may carry spatial structure across regions that broadens null distributions (Supplementary Fig. 27), reducing statistical power. This could explain the fewer significant gene cross-loadings in medicated (and consequently all) cases. Consistently, we observed greater variability in individual-level contributions to gene cross-loadings among medicated compared to unmedicated cases (Supplementary Fig. 26). These findings underscore that clinical factors, frequently overlooked in spatial association studies, can substantially influence observed relationships; future work with more granular clinical data are needed to disentangle this influence.

Enrichment analyses of CCA-derived transcriptomic signatures revealed distinct signals from excitatory neurons across both prenatal and postnatal periods (Fig. 7). Several lines of evidence implicate excitatory neurons in the pathophysiology of OCD: genome-wide studies have identified risk variants in genes related to excitatory synapses[50]; in animal models, altering excitatory cortico-striatal input (via Sapap3 or Slitrk5 knockouts) drives compulsive grooming that resolves when excitatory input is normalized[73,74]; and MR spectroscopy at 7 T demonstrates elevated glutamate in frontal cortex in OCD[75]. The

implication of prenatal gene expression from excitatory neurons, especially in unmedicated patients, suggests disruptions in these cells early in neurodevelopment. The more significant enrichment for postnatal excitatory neuron signatures in medicated patients suggests that structural alterations associated with medication status may also involve these cells.

To contextualize the spatial associations identified by CCA within OCD genetics, we assessed contributions from genes differentially expressed in OCD using in vivo dorsolateral prefrontal cortex tissue collected intraoperatively from patients and neurological controls undergoing deep brain stimulation. Genes down-regulated showed significant contributions to the spatial associations (Fig. 7). Differentially expressed genes in postmortem caudate and nucleus accumbens tissue, reported in previous studies[48,49], also contributed. These results corroborate the transcriptomic signatures identified by CCA. Enrichment of OCD risk genes identified in the largest GWAS to date[50] was only nominally significant in unmedicated patients. This attenuated enrichment may reflect the fact that GWAS-identified genes to date represent only a fraction of OCD-associated variants, estimated to exceed 11,000[50]. Clarifying the mechanistic links between common genetic variants, gene expression, and structural alterations will require future studies that combine individual-level genomic, transcriptomic, and neuroimaging data.

This study had limitations. First, neuroimaging samples were collected without harmonized acquisition protocols, contributing to data heterogeneity. To address this, we used NeuroCombat[26] for harmonization and adjusted for varying scan quality using the Euler number[27]; we found similar results when using linear mixed-effects models for harmonization (Supplementary Figs. 18–20). Second, medication status was a binary variable on the day of the scan, but details of dosage, duration, specific medications, and usage history that would provide greater granularity for assessing medication effects were not available. Third, our machine learning analyses used clinical measures that similarly lacked granularity, which could have limited the performance of machine learning models. Among these variables, onset was categorized as early or late rather than using specific ages, and anxiety and depression were binary variables rather than continuous measures of symptom severity. Fourth, in the functional contextualization analyses, subcortical regions were assigned to functional networks if any voxel within the region was associated with a network. This was necessary to align voxel-level network assignments from the Cole-Anticevic atlas[30] with the vertex- or region-level resolution of the subcortical phenotypes in this study. Fifth, the AHBA dataset used in the CCA includes data from only six healthy donors, with reduced variability in sex (five males and one female), ethnicity, cause of death, and postmortem interval; this limits the representativeness of its gene expression measures. We mitigated this limitation by focusing on the three transcriptional components with the highest reproducibility across donors and across independent gene expression datasets. Nonetheless, validation will ultimately require additional transcriptomic datasets based on larger and more demographically diverse samples. In addition, given the descriptive nature of the CCA, these findings should be interpreted primarily as reflecting spatial correspondence between structural alterations and normative gene expression gradients, rather than as direct evidence of transcriptomic or cellular mechanisms underlying the structural alterations observed in OCD, which will require further investigation in future studies. Sixth, the sample size for our in vivo gene expression analysis in OCD was limited, thereby reducing statistical power. We are actively working on increasing the sample size of this important dataset for future studies. Finally, this structural neuroimaging study primarily provides a descriptive characterization of the structural correlates of OCD. Although we used several complementary approaches to probe potential functional and biological underpinnings, these analyses are primarily hypothesis-generating. Future studies integrating additional and complementary neuroimaging and genetic modalities will be required to confirm and further elucidate the potential relationships suggested here between structural alterations and their functional and biological correlates.

Ultimately, we expect that probing expanded neuroimaging phenotypes, as well as developing novel ones, in structural and other neuroimaging modalities, will advance the deciphering of the enigma of mental illness and cognitive-behavioral traits.

Methods

Participants and clinical characterization

This study included 47 datasets from 26 international sites participating in the ENIGMA-OCD. Each dataset contained demographic, clinical, and structural neuroimaging data from OCD cases and neurotypical controls. Biological sex was available from the demographic records provided by each site; gender was not systematically collected and was not analyzed. Detailed demographic and clinical information for each dataset are provided in Supplementary Tables 1 and 2–7, respectively. We initially considered data from 4554 participants. After excluding 35 participants due to poor preprocessing results (Quality Control), our final sample consisted of 2255 OCD cases and 2264 healthy controls. All local institutional review boards approved the use of anonymized data for this analysis. Participant compensation, when provided, was determined locally at each contributing site. Importantly, participating sites shared only preprocessed neuroimaging results, not raw neuroimaging data.

Diagnoses of psychiatric disorders, including OCD and comorbid conditions, were made according to DSM-IV(-TR) or DSM-5 criteria in structured interviews. Medication status (unmedicated vs medicated) was determined based on medication use at the time of the scan. OCD severity was measured using the Yale-Brown Obsessive Compulsive Scale (Y-BOCS) for adults and the Children's Y-BOCS for younger participants[76–78]. OCD onset was classified as early if it occurred before age 18, and late if it began at 18 or older. OCD illness duration was measured in years since diagnosis. Comorbid depression was defined as the current presence of major depressive disorder, and comorbid anxiety was defined by the current presence of any anxiety disorder.

MRI acquisition and preprocessing

T1-weighted (T1w) MRI data were acquired using 1.5 or 3 tesla scanners and were preprocessed locally using a containerized pipeline that fixed the software environment across sites to ensure consistency across local environments. The acquisition parameters for each sample are provided in Supplementary Table 8. MRI scans underwent standard preprocessing using recon-all from FreeSurfer versions 7.1.1, 7.2, or 7.3.2[79], which are documented to produce identical results when using default settings, as used in this study. Preprocessing steps included non-uniformity correction, skull stripping, segmentation of tissue and subcortical structures, and cortical surface reconstruction. In addition, the ENIGMA Shape Analysis pipeline[22–24] was used to estimate surface meshes for seven bilateral subcortical structures: amygdala, caudate nucleus, hippocampus, nucleus accumbens, pallidum, putamen, and thalamus. This pipeline computes surface meshes from the boundaries of the subcortical structure segmentations generated by FreeSurfer. These meshes are then registered to a pre-computed average template by first aligning the mean and Gaussian curvatures to the template, followed by a refinement step that aligns the medial curve of each structure to the template.

Quality control

Quality control was performed to ensure high-quality neuroimaging data and minimize the impact of scan quality variability on analyses. Our preprocessing pipeline produced comprehensive visual reports that included snapshots of surface reconstructions and volume segmentations generated by FreeSurfer overlaid on MRI images in axial,

coronal, and sagittal views across several slices. The reports also included similar snapshots and 3D renderings of subcortical surfaces derived using the ENIGMA Shape Analysis pipeline. These visual reports were reviewed by a neuroimaging expert at the coordinating site (Yale University) upon receipt of neuroimaging data preprocessing results. In addition, scans with an Euler number lower than two median absolute deviations (MAD) from the dataset-specific median were re-examined. Scans showing substantial abnormalities, inaccurate segmentation or surface estimation for cortical and subcortical regions were excluded from further analysis. Finally, the Euler number was included as a covariate in all analyses to control for variability in scan quality[27].

Structural neuroimaging phenotypes

Nine structural neuroimaging phenotypes were estimated for cortical regions and four for subcortical structures, including thalamus, amygdala, caudate nucleus, putamen, nucleus accumbens, hippocampus, and globus pallidus. For each cortical region, eight structural phenotypes (the ninth is described below) were derived from FreeSurfer's recon-all pipeline: surface area, thickness, gray matter volume, Gaussian curvature, mean curvature, curvature index, folding index, and sulcal depth. Volume was also derived for subcortical structures. In addition, two vertex-wise measures, the logarithm of the Jacobian determinant and radial distance, were computed for subcortical regions as part of the ENIGMA Shape Analysis pipeline. The Jacobian determinant represents the surface dilation ratio between the subcortical structure and a template at a corresponding vertex, serving as a proxy for surface area. The radial distance represents the distance between a vertex on the surface of the subcortical structure and its medial curve (i.e., the curve that passes through the center of a three-dimensional structure).

We estimated two networks measuring pairwise structural similarity across regions for each participant. The morphometric inverse divergence (MIND) networks were estimated as in Sebenius et al.[25], by calculating the inverse of the multivariate Kullback–Leibler (KL) divergence between the standardized vertex-wise measures of two regions. Briefly, given regions a and b, with vertices V_a and V_b, and corresponding multivariate distributions P_a and P_b over vertex-wise morphometric feature vectors, the KL divergence between P_a and P_b is estimated using the k-nearest neighbor divergence approximation by Perez-Cruz[80]:

$$\hat{D}_{\mathrm{KL}}(P_a||P_b) = -\frac{d}{n}\sum_{i=1}^{n}\log\frac{r_k(x_i)}{s_k(x_i)} + \log\frac{m}{n-1} \tag{1}$$

where d is the number of structural features, n is the number of vertices in V_a, and m is the number of vertices in V_b. For each vertex x_i, $r_k(x_i)$ is the distance to its k-th nearest neighbor in V_a (excluding x_i), and $s_k(x_i)$ is the distance to its k-th nearest neighbor in V_b. The method uses $k=1$ and leverages k-d trees to efficiently compute nearest neighbors.

Because KL divergence is asymmetric, and to avoid potential negative estimates, a symmetric version is defined as:

$$\hat{D}(P_a, P_b) = \max\left(\hat{D}_{\mathrm{KL}}(P_a||P_b), 0\right) + \max(\hat{D}_{\mathrm{KL}}(P_b||P_a), 0) \tag{2}$$

Finally, the MIND similarity metric is computed as:

$$\mathrm{MIND} = \frac{1}{1+\hat{D}(P_a, P_b)} \tag{3}$$

For computing the MIND network for each participant, standardized vertex-wise measures of surface area, cortical thickness, volume, mean curvature, and sulcal depth were used[16]. Filtering to remove vertices with null values was not applied, thereby enabling consistent analyses across this and other neuroimaging phenotypes.

Furthermore, we used the same similarity measure to standardized vertex-wise measures of the logarithm of the Jacobian determinant and radial distance from the ENIGMA Shape Analysis pipeline to estimate structural similarity between subcortical regions, naming the resulting network the subcortical MIND (scMIND).

Univariate statistical analyses

Linear modeling of case-control differences in regional neuroimaging phenotypes. Linear regression models were used to compare neuroimaging phenotypes between OCD cases and controls in each brain region. Subcortical surface area (log-Jacobian determinant) and radial distance were compared at each vertex, consistent with previous studies[81–85]. Neuroimaging data were first harmonized across datasets with NeuroCombat[26], preserving the effects of diagnosis, age, and sex. In each model, the dependent variable represented the neuroimaging phenotype of a brain region, while the independent variables were diagnosis (OCD vs. control), age, sex, Euler number, and total intracranial volume. Total intracranial volume was included in all models to maintain a consistent covariate structure and improve comparability of results across neuroimaging phenotypes. We tested the single contrast for the main effect of OCD, yielding one scalar Cohen's d effect size for each model. Cohen's d was obtained using the following expression:

$$d = \frac{\mathbf{C}'\boldsymbol{\psi}}{\sqrt{\frac{\sum\boldsymbol{\epsilon}^2}{N-\mathrm{rank}(\mathbf{M})}}} \tag{4}$$

where $\mathbf{C}$ is a $r\times s$ full-rank matrix of s contrasts, $\boldsymbol{\psi}$ is a $r\times 1$ vector of regression coefficients, $\boldsymbol{\epsilon}$ is the $N\times 1$ vector of residuals, $\mathbf{M}$ is the full-rank $N\times r$ design matrix that includes all effects of interest in addition to all modeled covariate effects. The denominator term corresponds to the standard deviation of model residuals.

Permutation inference for linear models. The Freedman-Lane procedure is a robust and flexible approach for permutation testing in linear models. It is particularly effective in scenarios involving nuisance variables (i.e., covariates), as it disrupts the relationship between the response variable and predictors of interest while preserving the relationship with nuisance variables. This method has been shown to provide strong control over type I error rates while maintaining statistical power[72].

The procedure begins by fitting a full model that includes both the predictors of interest and the nuisance variables, estimating the statistic of interest from the model coefficients. To construct permutation distributions for the statistic of interest while preserving the effects of nuisance variables, the procedure first fits a model using only the nuisance variables. It then generates permuted response variables by combining the non-permuted fitted values and permuted residuals from the nuisance-only model. The fitted values represent the variance explained by the nuisance variables and are not permuted to preserve their relationship with the response variable. The residuals represent the variance not explained by the nuisance variables, that is left to be accounted for by the predictors of interest, and are therefore permuted to break the relationship between the response variable and predictors of interest. These permuted response variables are then used to refit the full model multiple times, building a null distribution for the statistic of interest.

Formally, the Freedman-Lane method can be expressed as:

$$(\mathbf{PR_z} + \mathbf{H_z})\mathbf{Y} = \mathbf{X\beta} + \mathbf{Z\gamma} + \boldsymbol{\epsilon} \tag{5}$$

Where $\mathbf{P}$ is a $N \times N$ permutation matrix, $\mathbf{R_z} = \mathbf{I} - \mathbf{H_z}$ is the residual-forming matrix for the nuisance-only model, $\mathbf{H_z} = \mathbf{Z}(\mathbf{Z}^+)$ is the projection (or hat) matrix for the nuisance-only model, with the superscript (+) representing the Moore–Penrose pseudo-inverse. $\mathbf{Y}$ is the $N \times 1$ vector of observed data, $\mathbf{X}$ is a $N \times r$ matrix of predictors of interest, $\boldsymbol{\beta}$ is the $r \times 1$ vector of regression coefficients for predictors of interest, $\mathbf{Z}$ is an $N \times s$ matrix of nuisance variables, $\boldsymbol{\gamma}$ is an $s \times 1$ vector of regression coefficients for nuisance variables, and $\boldsymbol{\epsilon}$ is the $N \times 1$ vector of residuals. In the unpermuted case, $\mathbf{P}$ equals the identity matrix, making the left-hand term reduce to $\mathbf{Y}$.

Combining regional results with non-parametric combination

To assess the convergence of alterations across neuroimaging phenotypes within regions or vertices, and to map alterations in each phenotype onto functional networks, we combined *p*-values for case–control differences from region- or vertex-wise univariate linear models using non-parametric combination[31]. Specifically, *p*-values from linear models were combined using Fisher's method, which yields a single statistic that summarizes evidence against the null. Statistical significance was assessed using synchronized Freedman–Lane permutations applied to the set of linear models being combined, which preserves their dependence structure across permutations and ensures valid inference for the combined statistic.

Machine learning models for exploring brain-behavior associations

We used machine learning to examine whether structural neuroimaging phenotypes can predict clinical characteristics in OCD cases. For continuous outcomes, ridge regression was used, while logistic ridge regression was applied to dichotomous outcomes. Model performance was evaluated using 5-fold, 10-times repeated nested cross-validation, where the inner folds optimized regularization and the outer folds assessed model performance[86]. Specifically, the inner folds tuned the strength of L2 regularization in ridge and logistic regression models, with hyperparameters optimized over a log-spaced grid ranging from 10^{-4} to 10^{4}. This design ensures independent tuning of hyperparameters and evaluation of performance, thus avoiding overfitting. To avoid data leakage, harmonization and standardization of regional structural phenotypes were calculated using the training data and then applied to both the training and test sets[87]. Furthermore, to ensure that the detected associations were not influenced by covariates, we used linear models to estimate the effects of age, sex, Euler number, and total intracranial volume in the training dataset and then regressed out these effects from both the training and test datasets[88]. For vertex-wise neuroimaging phenotypes, we selected the top 1 percentile of predictors based on their highest F-statistic of association with the outcome measure at the start of each training fold, applying this selection to both the training and test sets to keep the number of predictors manageable. Model performance was assessed using Pearson correlation for continuous variables and Matthews correlation coefficient for dichotomous variables, as the latter is particularly effective for classification tasks with unbalanced classes[89]. Using correlation metrics for both models ensured consistency in performance comparability across continuous and dichotomous outcomes.

Permutation inference for machine learning

Permutation testing was used to assess the statistical significance of machine learning predictions[90]. In all machine learning models, the outcome variables were permuted before cross-validation, and the entire cross-validation procedure was repeated for the permuted case in exactly the same way as for the unpermuted case, avoiding violations of exchangeability.

To permute continuous outcome variables, the Freedman-Lane method was applied. In this method, a linear model was used to predict the outcome variable based solely on the covariates. A permuted outcome variable was then generated by adding the predicted values from this model to the permuted residuals. This method ensured the disruption of the relationship between the outcome and predictors while maintaining the association with covariates.

For binary outcome variables, the Manly method[91] was used. This method involves directly permuting the outcome variable. Formally, the logistic model fitted to the permuted outcome can be expressed as:

$$Pr((\mathbf{PY})_\mathbf{i} = \mathbf{1} | \mathbf{X_i}, \mathbf{Z_i}) = \frac{\mathbf{1}}{\mathbf{1} + \mathbf{e}^{-(\mathbf{X_i}\boldsymbol{\beta} + \mathbf{Z_i}\boldsymbol{\gamma})}} \quad (6)$$

where Pr denotes probability, i indexes a vector element or matrix row corresponding to a single participant/observation, $\mathbf{P}$ is a $N \times N$ permutation matrix, $\mathbf{Y}$ is the $N \times 1$ vector of observed data, $\mathbf{X}$ is a $N \times r$ matrix of predictors of interest, $\boldsymbol{\beta}$ is the $r \times 1$ vector of regression coefficients for predictors of interest, $\mathbf{Z}$ is an $N \times s$ matrix of nuisance variables, and $\boldsymbol{\gamma}$ is an $s \times 1$ vector of regression coefficients for nuisance variables. In the unpermuted case, $\mathbf{P}$ equals the identity matrix, so $(\mathbf{PY})_\mathbf{i}$ reduces to $\mathbf{Y_i}$.

Allen Human Brain Atlas preprocessing

The Allen Human Brain Atlas (AHBA) contains gene expression data from 3702 brain samples in MNI space, collected from six postmortem brains (5 male, 1 female; mean age = 42.5)[40]. We preprocessed the AHBA data following the standardized pipeline by Dear et al.[41], which yields three transcriptional components generalizable across donors and other datasets. As data from the right hemisphere is only available for two brains, the estimation of these components is restricted to the left hemisphere. We focused our analysis on the HCP-MMP parcellation, as it was the primary parcellation used to validate the pipeline.

Briefly, preprocessing of the AHBA data was conducted using the abagen package[92], which included filtering for cortical samples, mirroring right hemisphere samples from two brains to the left hemisphere to improve coverage, and removing probes that did not exceed background noise in at least 50% of samples. The remaining probes were aggregated to the gene level by selecting the most stable probe based on differential stability across donors. Sample locations were matched to brain regions within a 2 mm tolerance using the voxel-mass algorithm from abagen. Using the scaled robust sigmoid method, samples were first normalized across all genes, followed by gene normalization across all samples, before aggregating gene expression across donors.

Following preprocessing, genes were filtered based on differential stability, keeping the top 50% of genes based on average correlation of expression vectors across donors. Regions were also filtered to retain those sampled in at least three donors, resulting in 137 of the 180 HCP-MMP left hemisphere regions. Finally, dimension reduction was performed with diffusion map embedding[93], using a normalized cosine kernel without sparsity, with α set to 1. The first three components with the highest concordance across donors were retained, as in Dear et al.[41].

Canonical correlation analysis

To spatially associate brain structure disruptions in OCD with the three transcriptional components derived from the AHBA, we used CCA as implemented in Winkler et al.[94]. The CCA models linked two variable sets, both using the 137 regions of the left hemisphere from the HCP-MMP parcellation as observations. The first set comprised case-control brain maps, where each value represented the Cohen's *d* for the main effect of OCD on a brain region for a neuroimaging phenotype, as estimated from linear models. The second set consisted of the three transcriptional components, with each value reflecting the score of a region for a given component. CCA was estimated via QR decomposition of the input matrices, followed by singular value

decomposition of the inner product of the resulting orthogonal matrices. Canonical (i.e., latent) variables for each set were obtained by multiplying the canonical weights with the original variables. Cross-loadings were calculated as the Pearson correlation between each original variable and the canonical variable from the opposite set.

To ensure the robustness and stability of the CCA models and to rigorously evaluate statistical significance, we implemented two methodological frameworks, detailed below.

Feature selection for maximal generalizability and stability. To select the neuroimaging phenotypes to include in the CCA models while avoiding overfitting and ensuring stability, we employed a split-half cross-validation approach. OCD cases and controls were evenly divided into training and test sets, maintaining the proportion of cases, controls, and datasets in each split. Neuroimaging data harmonization was estimated using the training set and applied to both the training and test sets. Linear models were used within each set to calculate Cohen's *d* for case-control differences across regions for each neuroimaging phenotype. A CCA model linking case-control differences to the AHBA components was estimated using the training set and subsequently used to project the test set case-control differences and compute the first canonical correlation with the AHBA components. The process was repeated after swapping the training and test sets and performed 25 times, resulting in a total of 50 iterations. Generalizability of associations was assessed by averaging the first out-of-sample canonical correlations across iterations, while stability was evaluated by calculating pairwise correlations between the concatenated left and right weights of CCA models from the training sets. Performance was determined as the average of generalizability and stability. We repeated this procedure for all possible combinations of neuroimaging phenotypes, selecting the one that maximized performance.

Assessing statistical significance with surrogate brain maps from permutations of linear models. After determining the optimal set of neuroimaging phenotypes, we fit CCA models using the entire sample. The statistical significance of spatial associations has been typically assessed using methods such as spatial permutations (commonly referred to as spin tests)[95] or spatially parameterized models[96,97]. However, these approaches rely on strong assumptions that can inflate false positive rates[43,44]. To circumvent the need for these methods, we used the Freedman-Lane procedure to generate surrogate brain maps that preserved the original spatial relationships while removing case-control effects. This method has been shown to adequately control false positive rates while maintaining statistical power and has been broadly used for linear model permutation in neuroimaging analyses[71,72]; we therefore applied it to spatial association testing. Specifically, regression models across all regions and neuroimaging phenotypes were simultaneously permuted, generating surrogate case-control brain maps that maintained spatial relationships while removing case-control differences. These surrogate maps were then used to assess the statistical significance of canonical correlations and cross-loadings.

Differential expression analysis in the in vivo OCD brain

Ethics. This study was approved by the Research Ethics Committee of the University of Sao Paulo School of Medicine and the Brazilian National Commission of Research Ethics (CAAE:32400620.7.0000.0068 and 14675413.9.0000.0068). All participants provided written informed consent for sample collection and RNA sequencing. Participants received compensation in accordance with local institutional procedures.

Participants. In vivo brain samples were collected during procedures for deep brain stimulation (DBS) electrode implantation at the University of Sao Paulo School of Medicine. These comprised 4 samples from three OCD cases and 6 from four neurological controls, including two individuals with dystonia and two with Parkinson's disease. Psychiatric diagnoses for all participants were determined by a trained clinician using the SCID-IV. Neurological controls had no current, past, or family history of OCD. All participants were adults (aged over 18 years). Biological sex was recorded for all participants during clinical interviews; gender was not collected for this study. Detailed demographic characteristics of the participants are provided in Supplementary Table 9. DBS was indicated based on standard criteria for each condition[6,98,99].

All participants have been regularly monitored since the procedure for tissue collection, and no adverse events related to it have been observed.

Tissue collection and RNA extraction. Standardized 0.3 cm^3 samples were collected from the dorsolateral prefrontal cortex during electrode implantation. In the routine DBS procedure, this region is cauterized to control bleeding when a cannula is inserted to guide the electrode to its target. For the study, a microdissector was used to collect a sample from this region—that is, tissue that would otherwise have been destroyed by cauterization— and then hemostatic cautery was applied to the margins so that the cortical surface was prepared exactly as in the standard clinical procedure. With the margins cauterized, the neurosurgeon placed the tissue samples directly into an Eppendorf tube on dry ice, containing 250 μL of Allprotect Tissue Reagent (Qiagen, Germany). The samples were then immediately transported to the research laboratory and stored at − 20 °C for up to 7 days. RNA extraction was performed using the AllPrep RNA Mini Kit (Qiagen, Germany), following the manufacturer's instructions. After RNA extraction, the samples were stored at − 80 °C.

RNA sequencing. To minimize batch effects, all samples were RNA sequenced at the Yale Center for Genomic Analysis. Prior to sequencing, RNA integrity was assessed with the 2100 BioAnalyzer System (Agilent, Santa Clara, USA). All samples had RIN values above 6.5, with a mean RIN of 7.5. Strand-specific RNA sequencing libraries were generated following rRNA and globin depletion using the Globin-Zero Gold kit (Illumina, San Diego, CA) according to the manufacturer's instructions. Libraries were sequenced on an Illumina NovaSeq 6000 System (Illumina, San Diego, CA) with 100 bp paired-end reads at a depth of approximately 105 million read pairs per sample (actual range: 98–113 million).

Preprocessing of RNA sequencing data. All RNA sequencing data were processed at the Icahn School of Medicine at Mount Sinai. Reads were aligned to the GRCh38 primary assembly with Gencode v30 annotation using STAR[100] (2.7.2a), followed by sorting with samtools[101] (1.13) and duplicate marking with Picard Tools (2.20.1). Gene-level quantification was performed using featureCounts[102] (1.6.3). Quality control metrics from FASTQC, featureCounts, and Picard were compiled and visually inspected.

Differential gene expression analysis. Differential gene expression analysis was performed in R using edgeR[103] (3.40.2), variancePartition[104] (1.28.9), sva[105] (3.46.0), and limma[106] (3.54.2) packages. Transcripts were filtered to retain only Ensembl genes with counts per million (CPM) greater than 0.1 in at least five samples, resulting in 13,827 transcribed genes for subsequent analyses. Normalization for library size was conducted using the trimmed mean of M-values (TMM) method implemented in the calcNormFactors function from edgeR[107]. To prepare the data for linear modeling, the voomWithDreamWeights function from variancePartition was used to transform the counts to $\log_2(\text{CPM} + 0.5)$ and to estimate precision weights for each sample, accounting for heteroscedasticity in the

count data. Surrogate variable analysis was conducted using the sva function from the sva package on the gene expression measures to detect hidden confounding factors, leading to the identification of one surrogate variable. Differential gene expression analysis was then performed using linear mixed-effects models implemented in the dream function from variancePartition[108]. The models were adjusted for age, sex, RNA integrity number (RIN), and the surrogate variable as fixed effects, and included subject as a random effect with a random intercept. Subsequently, the eBayes function from limma was employed to fit an empirical Bayes model, stabilizing variance estimates across genes.

Enrichment analysis

We performed enrichment analysis of the gene cross-loadings obtained from CCA. For each gene set tested, the enrichment score was calculated as the average cross-loading of genes within the set that overlapped with the 7973 genes retained in the preprocessed AHBA dataset. Statistical significance was assessed using surrogate case-control brain maps. Specifically, enrichment scores were recalculated from cross-loadings derived from these maps to generate surrogate distributions for comparison against observed enrichment scores, ensuring consistency with the null hypothesis used in the spatial association analysis of CCA and cross-loadings. Gene sets for the enrichment analysis were determined by overlapping the gene sets detailed below with the 7973 genes available in the preprocessed AHBA dataset.

Cell-type. To identify genes expressed by prenatal and postnatal cell types, we used single-cell and single-nucleus gene expression data from the PsychENCODE. A brief description of the datasets is provided below, with additional details on data collection and preprocessing available in the respective publications:

- Prenatal gene expression: single-cell RNA-seq data from 9 samples, each from a different individual (6 males and 3 females; age range: 5 postconception weeks to 125 days), spanning 4 brain regions (pallium, neocortex, cortical plate, and dorsal frontal cortex)[46].
- Postnatal gene expression: single-nucleus RNA-seq data from 166 samples, each from a different neurotypical control (111 males and 55 females; age range: 2 to 89 + years) of diverse ancestries, obtained from the prefrontal cortex[47].

Each dataset was preprocessed to associate genes with specific cell types. Genes with nonunique names or no expression in any cell type were excluded. Gene expression values were log-transformed with a pseudocount and normalized. Average cell-type-specific gene expression values were then calculated. For each cell type, we selected the top 10% of genes with the highest average expression levels for enrichment analysis.

Gene expression studies of OCD. We compiled lists of genes implicated in OCD by multiple genetic studies, detailed as follows:

- Differential expression analysis in in vivo brain tissue: Genes identified as significantly differentially expressed (FDR-adjusted) in the dorsolateral prefrontal cortex, identified in the differential expression analysis described in the section Differential expression analysis in the in vivo OCD brain.
- Differential expression analyses in postmortem brain tissue: Differential expression analysis was conducted in two prior studies using postmortem brain samples from OCD cases and controls. In Piantadosi et al.[48], samples from 7 OCD cases and 8 controls were collected from the head of the caudate nucleus, the nucleus accumbens, and the medial and lateral orbitofrontal cortices. However, only the caudate nucleus and nucleus accumbens showed significant differential expression (FDR-adjusted) and were included in the enrichment analysis. In Lisboa et al.[49], samples from 6 OCD cases and 8 controls were collected from the caudate nucleus, nucleus accumbens, and putamen. Statistically significant (FDR-adjusted) differential gene expression was found in all of these regions, and these genes were included in the enrichment analysis.

This enrichment analysis tests whether genes implicated in OCD through differential expression analyses in single brain regions also contribute to the brain-wide transcriptional signature identified by CCA. The former provides more direct evidence of gene involvement in OCD but is agnostic to macroscale brain alterations, while the latter is linked to OCD-related structural alterations but via indirect association. As such, this analysis bridges complementary evidence across scales.

Genome-wide association study of OCD. To assess whether genes affected by common variants in OCD contribute to the brain-wide transcriptomic patterns identified by CCA, we compiled the 25 putative causal genes identified in the largest genome-wide association study of OCD to date, which included 53,660 cases and 2,044,417 controls[50]. These genes were prioritized using six complementary gene-mapping approaches in that study.

Statistics and reproducibility. No statistical method was employed to predetermine the sample size for our neuroimaging analyses because the study analyzed previously collected data; however, our sample size is consistent with those used in previous ENIGMA-OCD studies. No statistical method was used to predetermine the sample size for the differential expression analysis of in vivo brain samples; sample availability was constrained by the number of clinically indicated deep brain stimulation procedures during the study period, and all eligible samples were included. Permutation testing was conducted using 10,000 permutations. Multiple testing corrections were performed using the false discovery rate (FDR) with the Benjamini-Hochberg procedure. To compute permutation-derived p-values with high precision, making them suitable for FDR correction, we approximated the tails of the null distribution using a generalized Pareto distribution[109,110]. Specifically, this approximation was done for p-value < 0.1, and with the unpermuted statistic excluded from the null distribution when estimating the approximation. For CCA specifically, given that FDR has been shown to produce inadmissible results in this context, family-wise error correction was first applied within each CCA using the distribution of the maximum statistic[94], followed by Bonferroni correction to adjust for multiple CCAs.

To ensure the reproducibility of our results, we adopted various validation strategies: using linear models that included interaction terms between diagnosis and available clinical variables to support our choice of medication status, rather than other clinical variables, for stratifying OCD cases; comparing harmonization with NeuroCombat to harmonization using linear mixed-effects models; leave-k-datasets-out analysis to assess the stability of regional case-control effects; 5-fold, 10-times repeated cross-validation for machine learning; and split-half cross-validation for spatial CCA.

Reporting summary

Further information on research design is available in the Nature Portfolio Reporting Summary linked to this article.

Data availability

The individual-level neuroimaging and clinical data analyzed in this study are available under controlled access. Access is controlled because the data consist of sensitive personal information collected under specific informed consent and local Institutional Review Board (IRB) approval at each site. These authorize only secondary use that has been reviewed and approved by the principal investigator of each contributing site, subject to terms that circumscribe use of the data to the approved analyses, prohibit data redistribution, and require

compliance with the applicant's local IRB. Access to the data can be requested by contacting the ENIGMA-OCD Working Group chair, Odile van den Heuvel, at oa.vandenheuvel@amsterdamumc.nl, or the ENIGMA Consortium principal investigator, Paul Thompson, at pthomp@usc.edu, subject to approval by each contributing site's principal investigator. There are no restrictions on who may apply. Requests are typically responded to within 2 weeks. The RNA-seq data generated from in vivo brain tissue collected during deep brain stimulation in this study have been deposited in the Gene Expression Omnibus (GEO) database under accession code GSE328351. Results from the regional case–control difference analyses across neuroimaging phenotypes and the differential expression analyses of the RNA-seq dataset are provided in a Supplementary Data file and are also available on Figshare at https://figshare.com/s/85ae27b391d1d0a24a7c. The Cole-Anticevic functional atlas can be accessed at https://github.com/ColeLab/ColeAnticevicNetPartition. Preprocessed gene expression data from the Allen Human Brain Atlas, mapped to the HCP-MMP parcellation and including the three components derived using diffusion map embedding, are available at https://github.com/richardajdear/AHBA_gradients. Prenatal single-cell RNA-seq data from PsychENCODE provided by Li et al.[46] can be accessed at http://development.psychencode.org. Postnatal single-nucleus RNA-seq data provided by Emani et al.[47] are available at https://brainscope.gersteinlab.org. Differential expression results based on postmortem brain tissue (Piantadosi et al.[48] and Lisboa et al.[49]) and GWAS findings (Strom et al.[50]) are available in their respective publications. Source data are provided in this paper.

Code availability

Code implementing the methods used in this study is publicly available at GitHub (https://github.com/csleo95/Multi-phenotype-morphometry; archived release DOI: 10.5281/zenodo.19770466) and as a reproducible Code Ocean capsule (https://doi.org/10.24433/CO.7065197.v1). Code for MIND calculation using subjects processed through FreeSurfer can be accessed at https://github.com/isebenius/MIND. The ENIGMA Shape Analysis pipeline can be downloaded at https://enigma.ini.usc.edu/ongoing/enigma-shape-analysis/. All analyses were performed using Python version 3.12.4 and R version 4.2.0. Main Python packages included numpy[111] (1.26.4), scikit-learn[112] (1.5.1), scipy[113] (1.14.0), pandas[114] (2.2.3), joblib[115] (1.4.2), matplotlib[116] (3.9.1), surfplot[117] (0.2.0), and pyvista[118] (0.44.2).

References

1. Baxter, L. R. et al. Local cerebral glucose metabolic rates in obsessive-compulsive disorder. A comparison with rates in unipolar depression and in normal controls. *Arch. Gen. Psychiatry* **44**, 211–218 (1987).
2. Baxter, L. R. Brain imaging as a tool in establishing a theory of brain pathology in obsessive compulsive disorder. *J. Clin. Psychiatry* **51**, 22–25 (1990).
3. Rauch, S. L. et al. Regional cerebral blood flow measured during symptom provocation in obsessive-compulsive disorder using oxygen 15-labeled carbon dioxide and positron emission tomography. *Arch. Gen. Psychiatry* **51**, 62–70 (1994).
4. Shephard, E. et al. Toward a neurocircuit-based taxonomy to guide treatment of obsessive-compulsive disorder. *Mol. Psychiatry* **26**, 4583–4604 (2021).
5. Miguel, E. C. et al. Evolution of gamma knife capsulotomy for intractable obsessive-compulsive disorder. *Mol. Psychiatry* **24**, 218–240 (2019).
6. Mar-Barrutia, L. et al. Deep brain stimulation for obsessive-compulsive disorder: A systematic review of worldwide experience after 20 years. *World J. Psychiatry* **11**, 659–680 (2021).
7. Stein, D. J. et al. Obsessive-compulsive disorder. *Nat. Rev. Dis. Prim.* **5**, 52 (2019).
8. Hirschtritt, M. E. et al. Obsessive-compulsive disorder: Advances in diagnosis and treatment. *JAMA* **317**, 1358–1367 (2017).
9. Warrier, V. et al. Genetic insights into human cortical organization and development through genome-wide analyses of 2,347 neuroimaging phenotypes. *Nat. Genet.* **55**, 1483–1493 (2023).
10. Boedhoe, P. S. W. et al. Cortical abnormalities associated with pediatric and adult obsessive-compulsive disorder: Findings from the ENIGMA obsessive-compulsive disorder working group. *Am. J. Psychiatry* **175**, 453–462 (2018).
11. Boedhoe, P. S. W. et al. Distinct subcortical volume alterations in pediatric and adult OCD: A worldwide meta- and mega-analysis. *Am. J. Psychiatry* **174**, 60–69 (2017).
12. Duncan, L. E. et al. How genome-wide association studies (GWAS) made traditional candidate gene studies obsolete. *Neuropsychopharmacology* **44**, 1518–1523 (2019).
13. Sullivan, P. F. & Geschwind, D. H. Defining the genetic, genomic, cellular, and diagnostic architectures of psychiatric disorders. *Cell* **177**, 162–183 (2019).
14. Karczewski, K. J. & Snyder, M. P. Integrative omics for health and disease. *Nat. Rev. Genet.* **19**, 299–310 (2018).
15. Van Essen, D. C. & Drury, H. A. Structural and functional analyses of human cerebral cortex using a surface-based atlas. *J. Neurosci.* **17**, 7079–7102 (1997).
16. Sebenius, I. et al. Structural MRI of brain similarity networks. *Nat. Rev. Neurosci.* **26**, 42–59 (2025).
17. Schmaal, L. The curse and opportunity of heterogeneity in the pursuit of psychiatric biomarkers. *World Psychiatry* **22**, 271–272 (2023).
18. Segal, A. et al. Regional, circuit and network heterogeneity of brain abnormalities in psychiatric disorders. *Nat. Neurosci.* **26**, 1613–1629 (2023).
19. Ben-Zion, Z. et al. Evaluating the evidence for brain-based biotypes of psychiatric vulnerability in the acute aftermath of trauma. *Am. J. Psychiatry* **180**, 146–154 (2023).
20. Dinga, R. et al. Evaluating the evidence for biotypes of depression: Methodological replication and extension of Drysdale et al. (2017). *NeuroImage Clin.* **22**, 101796 (2019).
21. Glasser, M. F. et al. A multi-modal parcellation of human cerebral cortex. *Nature* **536**, 171–178 (2016).
22. Gutman, B. A. et al. Maximizing power to track Alzheimer's disease and MCI progression by LDA-based weighting of longitudinal ventricular surface features. *Neuroimage* **70**, 386–401 (2013).
23. Gutman, B. A. et al. Medial demons registration localizes the degree of genetic influence over subcortical shape variability: An N= 1480 meta-analysis. *Proc. IEEE Int. Symp. Biomed. Imaging* **2015**, 1402–1406 (2015).
24. Gutman, B. A. et al. A Riemannian framework for intrinsic comparison of closed genus-zero shapes. *Inf. Process. Med. Imaging* **24**, 205–218 (2015).
25. Sebenius, I. et al. Robust estimation of cortical similarity networks from brain MRI. *Nature Neuroscience* **26**, 1461–1471 (2023).
26. Fortin, J.-P. et al. Harmonization of cortical thickness measurements across scanners and sites. *Neuroimage* **167**, 104–120 (2018).
27. Rosen, A. F. G. et al. Quantitative assessment of structural image quality. *Neuroimage* **169**, 407–418 (2018).
28. Fouche, J.-P. et al. Shape analysis of subcortical structures in obsessive-compulsive disorder and the relationship with comorbid anxiety, depression, and medication use: A meta-analysis by the OCD Brain Imaging Consortium. *Brain Behav.* **12**, e2755 (2022).
29. Greene, A. S. et al. Brain-phenotype models fail for individuals who defy sample stereotypes. *Nature* **609**, 109–118 (2022).
30. Ji, J. L. et al. Mapping the human brain's cortical-subcortical functional network organization. *Neuroimage* **185**, 35–57 (2019).
31. Winkler, A. M. et al. Non-parametric combination and related permutation tests for neuroimaging: NPC and Related

Permutation Tests for Neuroimaging. *Hum. Brain Mapp.* **37**, 1486–1511 (2016).
32. Chamberlain, S. R. et al. Orbitofrontal dysfunction in patients with obsessive-compulsive disorder and their unaffected relatives. *Science* **321**, 421–422 (2008).
33. Stern, E. R. et al. Resting-state functional connectivity between fronto-parietal and default mode networks in obsessive-compulsive disorder. *PLoS ONE* **7**, e36356 (2012).
34. Perera, M. P. N. et al. Exploring functional connectivity in large-scale brain networks in obsessive-compulsive disorder: a systematic review of EEG and fMRI studies. *Cereb. Cortex* **34**, https://doi.org/10.1093/cercor/bhae327 (2024).
35. Yu, J. et al. Convergent functional change of frontoparietal network in obsessive-compulsive disorder: a voxel-based meta-analysis. *Front. Psychiatry* **15**, 1401623 (2024).
36. Beucke, J. C. et al. Default mode network subsystem alterations in obsessive-compulsive disorder. *Br. J. Psychiatry* **205**, 376–382 (2014).
37. Gürsel, D. A. et al. Frontoparietal areas link impairments of large-scale intrinsic brain networks with aberrant fronto-striatal interactions in OCD: a meta-analysis of resting-state functional connectivity. *Neurosci. Biobehav. Rev.* **87**, 151–160 (2018).
38. Fitzgerald, K. D. et al. Error-related hyperactivity of the anterior cingulate cortex in obsessive-compulsive disorder. *Biol. Psychiatry* **57**, 287–294 (2005).
39. Bruin, W. B. et al. The functional connectome in obsessive-compulsive disorder: resting-state mega-analysis and machine learning classification for the ENIGMA-OCD consortium. *Mol. Psychiatry* **28**, 4307–4319 (2023).
40. Hawrylycz, M. J. et al. An anatomically comprehensive atlas of the adult human brain transcriptome. *Nature* **489**, 391–399 (2012).
41. Dear, R. et al. Cortical gene expression architecture links healthy neurodevelopment to the imaging, transcriptomics and genetics of autism and schizophrenia. *Nat. Neurosci.* **27**, 1075–1086 (2024).
42. García-San-Martín, N. et al. Molecular and micro-architectural mapping of gray matter alterations in psychosis. *Mol. Psychiatry* **30**, 1287–1296 (2025).
43. Koussis, N. C. et al. Generation of surrogate brain maps preserving spatial autocorrelation through random rotation of geometric eigenmodes. Preprint at https://doi.org/10.1101/2024.02.07.579070 (2024).
44. Markello, R. D. & Misic, B. Comparing spatial null models for brain maps. *Neuroimage* **236**, 118052 (2021).
45. Salvan, P. et al. Serotonin regulation of behavior via large-scale neuromodulation of serotonin receptor networks. *Nat. Neurosci.* **26**, 53–63 (2023).
46. Li, M. et al. Integrative functional genomic analysis of human brain development and neuropsychiatric risks. *Science* **362**, eaat7615 (2018).
47. Emani, P. S. et al. Single-cell genomics and regulatory networks for 388 human brains. *Science* **384**, eadi5199 (2024).
48. Piantadosi, S. C. et al. Transcriptome alterations are enriched for synapse-associated genes in the striatum of subjects with obsessive-compulsive disorder. *Transl. Psychiatry* **11**, 171 (2021).
49. Lisboa, B. C. G. et al. Initial findings of striatum tripartite model in OCD brain samples based on transcriptome analysis. *Sci. Rep.* **9**, 3086 (2019).
50. Strom, N. I. et al. Genome-wide analyses identify 30 loci associated with obsessive-compulsive disorder. *Nat. Genet.* **57**, 1389–1401 (2025).
51. Llinares-Benadero, C. & Borrell, V. Deconstructing cortical folding: genetic, cellular and mechanical determinants. *Nat. Rev. Neurosci.* **20**, 161–176 (2019).
52. Fernández, V. et al. Cerebral cortex expansion and folding: what have we learned? *EMBO J.* **35**, 1021–1044 (2016).
53. Fischl, B. et al. Cortical folding patterns and predicting cytoarchitecture. *Cereb. Cortex* **18**, 1973–1980 (2008).
54. Sasabayashi, D. et al. Anomalous brain gyrification patterns in major psychiatric disorders: a systematic review and transdiagnostic integration. *Transl. Psychiatry* **11**, 176 (2021).
55. White, T. et al. The development of gyrification in childhood and adolescence. *Brain Cogn.* **72**, 36–45 (2010).
56. Mahjani, B. et al. Genetics of obsessive-compulsive disorder. *Psychol. Med.* **51**, 2247–2259 (2021).
57. Brander, G. et al. Association of perinatal risk factors with obsessive-compulsive disorder: a population-based birth cohort, sibling control study. *JAMA Psychiatry* **73**, 1135–1144 (2016).
58. Seidlitz, J. et al. Morphometric similarity networks detect microscale cortical organization and predict inter-individual cognitive variation. *Neuron* **97**, 231–247.e7 (2018).
59. Morgan, S. E. et al. Cortical patterning of abnormal morphometric similarity in psychosis is associated with brain expression of schizophrenia-related genes. *Proc. Natl. Acad. Sci. USA* **116**, 9604–9609 (2019).
60. Li, J. et al. Cortical structural differences in major depressive disorder correlate with cell type-specific transcriptional signatures. *Nat. Commun.* **12**, 1647 (2021).
61. Seidlitz, J. et al. Transcriptomic and cellular decoding of regional brain vulnerability to neurogenetic disorders. *Nat. Commun.* **11**, 3358 (2020).
62. Dorfschmidt, L. et al. Human adolescent brain similarity development is different for paralimbic versus neocortical zones. *Proc. Natl. Acad. Sci. USA* **121**, e2314074121 (2024).
63. Park, I. et al. Cortical gyrification differences between early- and late-onset obsessive-compulsive disorder: neurobiological evidence for neurodevelopmentally distinct subtypes. *Psychol. Med.* **53**, 5976–5985 (2023).
64. van den Heuvel, O. A. et al. The major symptom dimensions of obsessive-compulsive disorder are mediated by partially distinct neural systems. *Brain* **132**, 853–868 (2009).
65. Yun, J.-Y. et al. Brain structural covariance networks in obsessive-compulsive disorder: a graph analysis from the ENIGMA Consortium. *Brain* **143**, 684–700 (2020).
66. Harrewijn, A. et al. Cortical and subcortical brain structure in generalized anxiety disorder: findings from 28 research sites in the ENIGMA-Anxiety Working Group. *Transl. Psychiatry* **11**, 502 (2021).
67. Pauls, D. L. et al. Obsessive-compulsive disorder: an integrative genetic and neurobiological perspective. *Nat. Rev. Neurosci.* **15**, 410–424 (2014).
68. Robbins, T. W. et al. Obsessive-compulsive disorder: puzzles and prospects. *Neuron* **102**, 27–47 (2019).
69. Kong, X.-Z. et al. Mapping cortical and subcortical asymmetry in obsessive-compulsive disorder: findings from the ENIGMA consortium. *Biol. Psychiatry* **87**, 1022–1034 (2020).
70. Hibar, D. P. et al. Significant concordance of genetic variation that increases both the risk for obsessive-compulsive disorder and the volumes of the nucleus accumbens and putamen. *Br. J. Psychiatry* **213**, 430–436 (2018).
71. Freedman, D. & Lane, D. A nonstochastic interpretation of reported significance levels. *J. Bus. Econ. Stat.* **1**, 292–298 (1983).
72. Winkler, A. M. et al. Permutation inference for the general linear model. *Neuroimage* **92**, 381–397 (2014).
73. Burguière, E. et al. Optogenetic stimulation of lateral orbitofronto-striatal pathway suppresses compulsive behaviors. *Science* **340**, 1243–1246 (2013).
74. Shmelkov, S. V. et al. Slitrk5 deficiency impairs corticostriatal circuitry and leads to obsessive-compulsive-like behaviors in mice. *Nat. Med.* **16**, 598–602 (2010).

75. Biria, M. et al. Cortical glutamate and GABA are related to compulsive behaviour in individuals with obsessive compulsive disorder and healthy controls. *Nat. Commun.* **14**, 3324 (2023).
76. Goodman, W. K. et al. The yale-brown obsessive compulsive scale. I. development, use, and reliability. *Arch. Gen. Psychiatry* **46**, 1006–1011 (1989).
77. Goodman, W. K. et al. The yale-brown obsessive compulsive scale. II. validity. *Arch. Gen. Psychiatry* **46**, 1012–1016 (1989).
78. Scahill, L. et al. Children's yale-brown obsessive compulsive scale: reliability and validity. *J. Am. Acad. Child Adolesc. Psychiatry* **36**, 844–852 (1997).
79. Fischl, B. FreeSurfer. *Neuroimage* **62**, 774–781 (2012).
80. Perez-Cruz, F. Kullback–Leibler divergence estimation of continuous distributions. In *2008 IEEE International Symposium on Information Theory* 1666–1670 (IEEE, 2008).
81. Ho, T. C. et al. Subcortical shape alterations in major depressive disorder: Findings from the ENIGMA major depressive disorder working group. *Hum. Brain Mapp.* **43**, 341–351 (2022).
82. Ching, C. R. K. et al. Mapping subcortical brain alterations in 22q11.2 deletion syndrome: Effects of deletion size and convergence with idiopathic neuropsychiatric illness. *Am. J. Psychiatry* **177**, 589–600 (2020).
83. Chye, Y. et al. Subcortical surface morphometry in substance dependence: An ENIGMA addiction working group study. *Addict. Biol.* **25**, e12830 (2020).
84. Roshchupkin, G. V. et al. Heritability of the shape of subcortical brain structures in the general population. *Nat. Commun.* **7**, 13738 (2016).
85. Wade, B. S. C. et al. Effect of electroconvulsive therapy on striatal morphometry in major depressive disorder. *Neuropsychopharmacology* **41**, 2481–2491 (2016).
86. Cawley, G. C. & Talbot, N. L. C. On over-fitting in model selection and subsequent selection bias in performance evaluation. *J. Mach. Learn. Res.* **11**, 2079–2107 (2010).
87. Rosenblatt, M. et al. Data leakage inflates prediction performance in connectome-based machine learning models. *Nat. Commun.* **15**, 1829 (2024).
88. Snoek, L., Miletić, S. & Scholte, H. S. How to control for confounds in decoding analyses of neuroimaging data. *Neuroimage* **184**, 741–760 (2019).
89. Chicco, D. et al. The Matthews correlation coefficient (MCC) is more reliable than balanced accuracy, bookmaker informedness, and markedness in two-class confusion matrix evaluation. *BioData Min.* **14**, 13 (2021).
90. Ojala, M. & Garriga, G. C. Permutation Tests for Studying Classifier Performance. *J. Mach. Learn. Res.* **11**, 1833–1863 (2010).
91. Manly, B. F. J. *Randomization, Bootstrap and Monte Carlo Methods in Biology* (CRC Press, 1997).
92. Markello, R. D. et al. Standardizing workflows in imaging transcriptomics with the abagen toolbox. *eLife* **10**, e72129 (2021).
93. Vos de Wael, R. et al. BrainSpace: a toolbox for the analysis of macroscale gradients in neuroimaging and connectomics datasets. *Commun. Biol.* **3**, 103 (2020).
94. Winkler, A. M. et al. Permutation inference for canonical correlation analysis. *Neuroimage* **220**, 117065 (2020).
95. Alexander-Bloch, A. F. et al. On testing for spatial correspondence between maps of human brain structure and function. *Neuroimage* **178**, 540–551 (2018).
96. Burt, J. B. et al. Hierarchy of transcriptomic specialization across human cortex captured by structural neuroimaging topography. *Nat. Neurosci.* **21**, 1251–1259 (2018).
97. Burt, J. B., Helmer, M., Shinn, M., Anticevic, A. & Murray, J. D. Generative modeling of brain maps with spatial autocorrelation. *Neuroimage* **220**, 117038 (2020).
98. Hariz, M. & Blomstedt, P. Deep brain stimulation for Parkinson's disease. *J. Intern. Med.* **292**, 764–778 (2022).
99. Rodrigues, F. B. et al. Deep brain stimulation for dystonia. *Cochrane Database Syst. Rev.* **1**, CD012405 (2019).
100. Dobin, A. et al. STAR: ultrafast universal RNA-seq aligner. *Bioinformatics* **29**, 15–21 (2013).
101. Li, H. et al. The Sequence Alignment/Map format and SAMtools. *Bioinformatics* **25**, 2078–2079 (2009).
102. Liao, Y. et al. featureCounts: an efficient general purpose program for assigning sequence reads to genomic features. *Bioinformatics* **30**, 923–930 (2014).
103. Robinson, M. D. et al. edgeR: a Bioconductor package for differential expression analysis of digital gene expression data. *Bioinformatics* **26**, 139–140 (2010).
104. Hoffman, G. E. & Schadt, E. E. variancePartition: interpreting drivers of variation in complex gene expression studies. *BMC Bioinform.* **17**, 483 (2016).
105. Leek, J. T. et al. The sva package for removing batch effects and other unwanted variation in high-throughput experiments. *Bioinformatics* **28**, 882–883 (2012).
106. Ritchie, M. E. et al. limma powers differential expression analyses for RNA-sequencing and microarray studies. *Nucleic Acids Res.* **43**, e47 (2015).
107. Robinson, M. D. & Oshlack, A. A scaling normalization method for differential expression analysis of RNA-seq data. *Genome Biol.* **11**, R25 (2010).
108. Hoffman, G. E. & Roussos, P. Dream: powerful differential expression analysis for repeated measures designs. *Bioinformatics* **37**, 192–201 (2021).
109. Winkler, A. M. et al. Faster permutation inference in brain imaging. *Neuroimage* **141**, 502–516 (2016).
110. Knijnenburg, T. A. et al. Fewer permutations, more accurate P-values. *Bioinformatics* **25**, i161–i168 (2009).
111. Harris, C. R. et al. Array programming with NumPy. *Nature* **585**, 357–362 (2020).
112. Pedregosa, F. et al. Scikit-learn: Machine Learning in Python. *J. Mach. Learn. Res.* **12**, 2825–2830 (2011).
113. Virtanen, P. et al. SciPy 1.0: Fundamental Algorithms for Scientific Computing in Python. *Nat. Methods* **17**, 261–272 (2020).
114. McKinney, W. Data structures for statistical computing in Python. In *Proceedings of the 9th Python in Science Conference*, 56–61 (2010).
115. Varoquaux, G. et al. joblib/joblib: 1.4.2. Zenodo https://doi.org/10.5281/zenodo.14915602 (2024).
116. Hunter, J. D. Matplotlib: A 2D graphics environment. *Comput. Sci. Eng.* **9**, 90–95 (2007).
117. Gale, D. J. et al. Surfplot: Publication-ready brain surface figures (v0.1.0). Zenodo https://doi.org/10.5281/zenodo.5567926 (2021).
118. Sullivan, C. B. & Kaszynski, A. A. PyVista: 3D plotting and mesh analysis through a streamlined interface for the Visualization Toolkit (VTK). *J. Open Source Softw.* **4**, 1450 (2019).

Acknowledgements

We are grateful to Joseph Buxbaum and Dorothy Grice for their support throughout the execution of this project.

Author contributions

Conceptualization and methodology: L.C.S., J.R.S., I.S., A.M.W., C.P. and C.C. Data analysis: L.C.S. Analysis supervision and substantive manuscript contributions: J.R.S., N.D., C.V., Y.T.C., H.P., C.S.-M., R.R.-G., P.M.T., D.J.S., O.A.v.d.H., A.M.W., E.C.M.F., C.P. and C.C. ENIGMA-OCD Working Group leadership: P.M.T., D.J.S. and O.A.v.d.H. ENIGMA-OCD neuroimaging data preprocessing, covariate provision and manuscript revision: N.D., C.d.R.-T., Y.A., P.A., S.H.A., A.Ant., A.Ara., P.D.A., S.B., N.B., M.C.B., F.B., I.B., B.Bra., B.Bre., J.B., M.C.-B., S.C., A.D.C., S.D., D.D., I.C.D., M.A.N.E., G.K.E., A.F., J.D.F., S.M.D.D.F., L.F.F., R.G., M.H., A.H., M.Q.H., C.H., H.H., A.J., M.K., J.S.K., L.L., C.L., M.M.-S., H.v.M., I.M.-Z., D.M.-C., J.M.M., L.M., P.M., E.M.-M.,

T.N., J.C.N., E.L.N., J.O., I.P., M.L.P., J.C.P., M.P.-P., F.Pir., Fe.Pir., T.S.P., C.-S.R.L., J.Y.C.R., D.v.R., Y.S., J.B.d.S.A., F.S., V.S., N.S., E.R.S., A.v.d.S., S.I.T., H.T., F.T.-M., C.V., D.V., D.J.V., G.V., Z.W., Y.D.v.d.W., G.v.W., Q.Z., R.G.S., C.S.-M., D.J.S., O.A.v.d.H., E.C.M.F., C.P., C.C. and the ENIGMA-OCD Working Group. RNA-seq data collection: F.G., A.C.L., M.O.L., V.R.R., R.I., and C.C. RNA-seq data preprocessing: L.C.S., T.V.F., M.F., A.W.C. and C.C. RNA-seq data analysis: L.C.S. and C.C.

Funding

L.C.S. was supported by the International OCD Foundation 2025 Jenike Young Investigator Award, NIH grant R01MH130609 (to C.P.), and Sao Paulo Research Foundation scholarships 2020/12484-6 and 2022/10207-0. J.R.S. was supported by Sao Paulo Research Foundation grants 2023/18337-3 and 2023/02538-0. N.D. was supported by the International OCD Foundation Innovator Award of 2021. Y.A. was supported by the Japan Society for the Promotion of Science (JSPS; KAKENHI) grant 23K14825. P.A. was supported by PI22/00752 from Instituto de Salud Carlos III and MAR22005 from Fundació La Marató. S.H.A. was supported by the Canadian Institutes of Health Research, the Canada Research Chairs Program, the University of Toronto, and the CAMH Foundation. A.A. was supported by the Portuguese Foundation for Science and Technology (grant 2020.08114.BD). P.D.A. was supported by the Ontario Brain Institute, the Hotchkiss Brain Institute, the Alberta Children's Hospital Foundation, and the Alberta Innovates Translational Health Chair in Child and Youth Mental Health, and holds a patent for SLCIAI Marker for Anxiety Disorder granted May 6, 2008. S.B. was supported by a Río Hortega grant (CM21/00278) from the Carlos III Health Institute (co-funded by the European Social Fund, Investing in Your Future). J.B. was supported by the European Union 7th Framework Program TACTICS consortium (grant 278948). J.C. was supported by the Portuguese Foundation for Science and Technology (grants DL 57/2016/CP1370/CT0066 and CEECINST/00117/2021/CP2784/CT0001). M.C.B. was supported by the Portuguese Foundation for Science and Technology (grant UIDP/4950/2020). A.D.C. was supported by a PhD scholarship from the Portuguese Foundation for Science and Technology (FCT; reference 2022.09472.BD). I.C.D. was supported by the Portuguese Foundation for Science and Technology (grants UIDP/4950/2020 and 2022.04701.PTDC). G.K.E. was supported by NIH grants R21/R33MH107589 and R01MH111794 (awarded to E.R.S.). A.F. was supported by a PhD scholarship from the Portuguese Foundation for Science and Technology (FCT; reference 2022.12528.BD). J.D.F. was supported by NIMH grant R01MH085900. L.F.F. was supported by Conselho Nacional de Desenvolvimento Científico e Tecnológico (#302526/2018-8), Fundação Carlos Chagas Filho de Amparo à Pesquisa do Estado do Rio de Janeiro (#CNE E-26/200.950/2021), and the D'Or Institute of Research and Education (IDOR). J.I. was supported by NIMH grant R01MH131022. M.K. was supported by the Brain Science Convergence Research Program through the National Research Foundation of Korea (NRF), funded by the Ministry of Science & ICT (grant RS-2023-00266120). L.L. was supported by the Marató Foundation grants 01/2010 and 091710. C.L. was supported by the National Research Foundation of South Africa. M.M.S. was supported by a PhD scholarship from the Portuguese Foundation for Science and Technology (FCT; reference 2020.07946.BD). D.M.C. was supported by the International OCD Foundation Breakthrough Grant, the Swedish Brain Foundation (Hjärnfonden; FO2017-0154 and FO2020-0139), and the Region Stockholm ALF Medicine funding program (20200137). P.M. was supported by Portuguese Foundation for Science and Technology projects UIDB/50026/2020, UIDP/50026/2020, and LA/P/0050/2020, and by project NORTE-01-0145-FEDER-000039 through the European Regional Development Fund. T.N. was supported by JSPS KAKENHI grant JP21K07547. J.C.N. was supported by the Department of Science and Technology (DST INSPIRE faculty grant IFA12-LSBM-26) and the Department of Biotechnology (BT/06/IYBA/2012). J.O. was supported by NIMH grants R01MH085900 and R01MH081864. J.C.P. was supported by NIMH grant R01MH081864. M.P.P. was supported by grant RYC2021-031228-I funded by MCIN/AEI/10.13039/501100011033 and by the European Union NextGenerationEU/PRTR. F.P. was supported by the Italian Ministry of Health (Ricerca Corrente 2024). Y.C.J.R. was supported by the Department of Science and Technology (SR/S0/HS/0016/2011) and the Department of Biotechnology (BT/PR13334/Med/30/259/2009). Y.S. was supported by AMED grants JP23wm0625001 and JP24wm0625204. J.B.S.A. was supported by a postdoctoral scholarship from Fundação Maria-Emília (Brazil). E.R.S. was supported by NIH grants R21/R33MH107589 and R01MH111794. S.I.T. was supported by NIH grant R01MH138569 (MEGA-OCD). H.T. was supported by JSPS KAKENHI grant JP22K15766. F.T.M. was supported by Conselho Nacional de Desenvolvimento Científico e Tecnológico, Coordenação de Aperfeiçoamento de Pessoal de Nível Superior, the D'Or Institute for Research and Education, and Fundação Carlos Chagas Filho de Amparo à Pesquisa do Estado do Rio de Janeiro. G.V. was supported by the Wellcome-DBT India Alliance grant 500236/Z/11/Z. C.V. was supported by the International OCD Foundation Innovator Award of 2021. Z.W. was supported by the Key Program of the National Natural Science Foundation of China (82230045). A.W. was supported by JSPS KAKENHI grant 21K15749. G.V.W. was supported by ZonMw grants 165.610.002 and 016.156.318. Y.T.C. was supported by Neumora Therapeutics (formerly BlackThorn Therapeutics). C.S.M. was supported by Instituto de Salud Carlos III (PI16/00889, PI19/01171), Departament de Salut (PERIS SLT006/17/249), Fundació Marató de TV3 (202201-31), Agència de Gestió d'Ajuts Universitaris i de Recerca (2021SGR01017), and Ministerio de Ciencia e Innovación (PID2022–139081OB-C21). R.R.G. was supported by the EMERGIA Junta de Andalucía program (EMERGIA20_00139), Plan de Consolidación (CNS2023-143647), and Plan de Generación de Conocimiento (PID2021-122853OA-I00) of the Agencia Estatal de Investigación. P.M.T. was supported by NIH grant R01MH138569 (MEGA-OCD). D.J.S. was supported by the South African Medical Research Council (SAMRC). O.A.H. was supported by the International OCD Foundation Innovator Award of 2021 and by NIMH grant R01MH138569-01 (MEGA-OCD). C.P. was supported by NIH grant R01MH116038. C.C. was supported by NIH grant 1K99MH128540-01.

Competing interests

A.Ant. is the founder, president, and board member of Manifest Technologies. P.A. has received funding from Boston Scientific, Johnson & Johnson, Casen Recordati, and Viatris as a lecturer and to attend medical conferences. J.B. has, in the past 3 years, served as a consultant, advisory-board member, and/or speaker for Takeda, Roche, Medice, Angelini, Neuraxpharm, and Servier; he is not an employee or shareholder of any of these companies and reports no other financial or material support, including expert testimony, patents, or royalties. J.D.F. receives consultation fees from NOCD, Inc. P.M. has, in the past 3 years, received grants, CME-related honoraria, or consulting fees from Angelini, AstraZeneca, Bial, Biogen, DGS-Portugal, CES, FCT, FLAD, Janssen-Cilag, Gulbenkian Foundation, Lundbeck, Springer Healthcare, Tecnimede, Viatris, and 2CA-Braga. D.M.-C. receives royalties for articles contributed to UpToDate, Inc., and is part-owner of Scandinavian E-Health AB (all outside the submitted work). Y.S. is an employee of XNef, Inc. R.G.S. holds a scientific productivity grant from the National Council for Scientific and Technological Development (#307386/2021-0). D.J.S. has, in the past 3 years, received consultancy honoraria from Discovery Vitality, Johnson & Johnson, Kanna, L'Oréal, Lundbeck, Orion, Sanofi, Servier, Takeda, and Vistagen. C.P. has, in the past 3 years, consulted for Biohaven Pharmaceuticals, Ceruvia Lifesciences, Freedom Biosciences, UCB BioPharma, Nobilis Therapeutics, Transcend Therapeutics, F-Prime Capital Partners, Madison Avenue Partners, and Lundbeck Therapeutics; received research support from Transcend, Freedom, and Biohaven; and holds equity in Alco Therapeutics, Biohaven Pharmaceuticals, and Mind Therapeutics, none of which relate to the current

work, and is an inventor on several unrelated patents. The remaining authors declare no competing interests.

Additional information

Supplementary information The online version contains supplementary material available at https://doi.org/10.1038/s41467-026-74153-2.

Correspondence and requests for materials should be addressed to Leonardo Cardoso Saraiva, Christopher Pittenger or Carolina Cappi.

Peer review information *Nature Communications* thanks the anonymous reviewers for their contribution to the peer review of this work. A peer review file is available.

Reprints and permissions information is available at http://www.nature.com/reprints

Publisher's note Springer Nature remains neutral with regard to jurisdictional claims in published maps and institutional affiliations.

Open Access This article is licensed under a Creative Commons Attribution-NonCommercial-NoDerivatives 4.0 International License, which permits any non-commercial use, sharing, distribution and reproduction in any medium or format, as long as you give appropriate credit to the original author(s) and the source, provide a link to the Creative Commons licence, and indicate if you modified the licensed material. You do not have permission under this licence to share adapted material derived from this article or parts of it. The images or other third party material in this article are included in the article's Creative Commons licence, unless indicated otherwise in a credit line to the material. If material is not included in the article's Creative Commons licence and your intended use is not permitted by statutory regulation or exceeds the permitted use, you will need to obtain permission directly from the copyright holder. To view a copy of this licence, visit http://creativecommons.org/licenses/by-nc-nd/4.0/.

© The Author(s) 2026

Leonardo Cardoso Saraiva[1,2] ✉, João R. Sato[3], Isaac Sebenius[4], Nadza Dzinalija[5,6], Carla del Río-Torné[7,8], Fábio Godinho[9], Antonio C. Lopes[2], Thomas V. Fernandez[10], Monicke O. Lima[2], Vanessa R. Ramos[2], Ricardo Iglesio[9], Yoshinari Abe[11,12], Pino Alonso[7,8,13], Stephanie H. Ameis[14,15], Alan Anticevic[16], Ana Araújo[17,18], Paul D. Arnold[19,20], Srinivas Balachander[21], Nerisa Banaj[22], Marcelo C. Batistuzzo[2,23], Francesco Benedetti[24,25], Irene Bollettini[25], Beatrice Bravi[25], Brian Brennan[26,27], Jan Buitelaar[28,29], Miguel Castelo-Branco[17,18], Sunah Choi[30], Ana D. Costa[31,32], Sara Dallaspezia[25], Damiaan Denys[33,34], Isabel C. Duarte[17,35], Marco A. N. Echevarria[2], Goi Khia Eng[36,37], Afonso Fernandes[31,32], Jamie D. Feusner[38,39,40], Martijn Figee[41], Sophie M. D. D. Fitzsimmons[5,6], Leonardo F. Fontenelle[42,43,44], Rachael Grazioplene[1], Minji Ha[30], Alejandro Hinojosa[45], Marcelo Q. Hoexter[2], Chaim Huijser[46,47], Hao Hu[48], Anthony James[49], Minah Kim[50,51], Jun Soo Kwon[52,53,54], Luisa Lazaro[13,55,56], Christine Lochner[57], Mafalda Machado-Sousa[31,32], Hein van Marle[33,34,58], Ignacio Martínez-Zalacaín[7,59], David Mataix-Cols[60,61], José M. Menchón[7,8,13], Luciano Minuzzi[62,63], Pedro Morgado[31,32], Emma Muñoz-Moreno[45], Tomohiro Nakao[64], Janardhanan C. Narayanaswamy[21,65], Erika L. Nurmi[66], Joseph O'Neill[66,67], Inkyung Park[30], Mary L. Phillips[68], John C. Piacentini[66], Maria Picó-Pérez[31,69], Fabrizio Piras[22], Federica Piras[22], Tjardo S. Postma[5,6], Chiang-shan R. Li[1,70], Janardhan Y. C. Reddy[21], Daan van Rooij[28,71], Yuki Sakai[11,72,73], Juliana B. de Salles Andrade[42], Freda Scheffler[74], Venkataram Shivakumar[75], Noam Soreni[63,76], Emily R. Stern[36,37,77], Anouk van der Straten[33,34,78], Sophia I. Thomopoulos[79], Hirofumi Tomiyama[64], Fernanda Tovar-Moll[42], Daniela Vecchio[22], Dick J. Veltman[5,6], Ganesan Venkatasubramanian[21], Chris Vriend[5,6], Zhen Wang[80], Ysbrand D. van der Werf[5,6], Guido van Wingen[33,34], Qing Zhao[80], ENIGMA-OCD Working Group*, Alexander W. Charney[41,81,82], Youngsun T. Cho[1,10], Roseli G. Shavitt[2], Helen Pushkarskaya[1], Carles Soriano-Mas[7,8,13], Rafael Romero-Garcia[83,84], Paul M. Thompson[79], Dan J. Stein[85], Odile A. van den Heuvel[5,6], Anderson M. Winkler[1,86], Euripedes C. Miguel Filho[2], Christopher Pittenger[1,10,70,87,88,89,98] ✉ & Carolina Cappi[90,98] ✉

[1]Department of Psychiatry, Yale University School of Medicine, New Haven, CT, USA. [2]Department of Psychiatry, University of São Paulo, São Paulo, Brazil. [3]Center of Mathematics, Computing and Cognition, Universidade Federal do ABC, Santo André, Brazil. [4]Department of Psychiatry, University of Cambridge, Cambridge, UK. [5]Amsterdam UMC, Vrije Universiteit Amsterdam, Department of Psychiatry, Department of Anatomy & Neurosciences, Amsterdam, The Netherlands. [6]Amsterdam Neuroscience, Compulsivity Impulsivity & Attention, Amsterdam, The Netherlands. [7]Psychiatry and Mental Health Group, Neuroscience Program, Bellvitge Biomedical Research Institute (IDIBELL), L'Hospitalet de Llobregat, Spain. [8]Department of Clinical Sciences, School of Medicine, University of Barcelona, L'Hospitalet de Llobregat, Spain. [9]Neurosurgery Division, Department of Neurology, Hospital das Clínicas, University of São Paulo Medicine School, São Paulo, SP, Brazil. [10]Yale Child Study Center, Yale University, New Haven, CT, USA. [11]Department of Psychiatry, Graduate School of Medical Science, Kyoto Prefectural University of Medicine, Kyoto, Japan. [12]Sugimoto Psychiatric Clinic, Kyoto, Japan. [13]Network Center for Biomedical Research on Mental Health (CIBERSAM), Carlos III Health Institute (ISCIII), Madrid, Spain. [14]Cundill Centre for Child and Youth Depression, Margaret and Wallace McCain Centre for Child, Youth and Family Mental Health, Centre for Addiction and Mental Health, Toronto, ON, Canada. [15]Department of Psychiatry, Temerty Faculty of Medicine, University of Toronto, Toronto, ON, Canada. [16]Janssen Research & Development, LLC, a Johnson & Johnson Company, Titusville, NJ, USA. [17]CIBIT, ICNAS, University of Coimbra, Coimbra, Portugal. [18]Faculty of Medicine, University of Coimbra, Coimbra, Portugal. [19]The Mathison Centre for Mental Health Research & Education, Hotchkiss Brain Institute, University of Calgary, Calgary, AB, Canada. [20]Departments of Psychiatry and Medical Genetics, Cumming School of Medicine, University of Calgary, Calgary, AB, Canada. [21]OCD Clinic, Department of Psychiatry, National Institute of Mental Health and Neurosciences (NIMHANS), Bangalore, India. [22]Laboratory of Neuropsychiatry, Department of Clinical Neuroscience and Neurorehabilitation, IRCCS Santa

Lucia Foundation, Rome, Italy. [23]Department of Methods and Techniques in Psychology, Pontifical Catholic University, São Paulo, SP, Brazil. [24]Vita-Salute San Raffaele University, Milano, Italy. [25]Psychiatry and Clinical Psychobiology, Division of Neuroscience, IRCCS Ospedale San Raffaele, Milano, Italy. [26]McLean Hospital, Belmont, MA, USA. [27]Harvard Medical School, Boston, MA, USA. [28]Radboudumc, Department of Medical Neuroscience, Nijmegen, The Netherlands. [29]Karakter Child and Adolescent Psychiatry University Centre, Nijmegen, The Netherlands. [30]Department of Brain and Cognitive Sciences, Seoul National University College of Natural Sciences, Seoul, Republic of Korea. [31]Life and Health Sciences Research Institute (ICVS), School of Medicine, University of Minho, Braga, Portugal. [32]Clinical Academic Center – Braga, Braga, Portugal. [33]Amsterdam UMC, location University of Amsterdam, Department of Psychiatry, Amsterdam, The Netherlands. [34]Amsterdam Neuroscience, Amsterdam, The Netherlands. [35]ICNAS, University of Coimbra, Coimbra, Portugal. [36]Department of Psychiatry, New York University Grossman School of Medicine, New York, NY, USA. [37]Nathan Kline Institute for Psychiatric Research, Orangeburg, NY, USA. [38]Division of Neurosciences & Clinical Translation, Department of Psychiatry, Temerty Faculty of Medicine, University of Toronto, Toronto, ON, Canada. [39]Centre for Addiction and Mental Health, Toronto, ON, Canada. [40]Department of Women's and Children's Health, Karolinska Institutet, Stockholm, Sweden. [41]Department of Psychiatry, Icahn School of Medicine at Mount Sinai, New York, NY, USA. [42]D'Or Institute for Research and Education (IDOR), Rio de Janeiro, RJ, Brazil. [43]Institute of Psychiatry, Federal University of Rio de Janeiro (IPUB/UFRJ), Rio de Janeiro, RJ, Brazil. [44]Department of Psychiatry, School of Clinical Sciences, Monash University, Clayton, VIC, Australia. [45]MRI Core Facility, IDIBAPS, Barcelona, Spain. [46]Levvel, Amsterdam, The Netherlands. [47]Amsterdam UMC, Department of Child and Adolescent Psychiatry, Amsterdam, The Netherlands. [48]Department of Psychiatry, Shanghai Mental Health Center, Shanghai Jiao Tong University School of Medicine, Shanghai, P.R. China. [49]Department of Psychiatry, University of Oxford, Warneford Hospital, Oxford OX3 7JX, UK. [50]Department of Psychiatry, Seoul National University College of Medicine, Seoul, Republic of Korea. [51]Department of Neuropsychiatry, Seoul National University Hospital, Seoul, Republic of Korea. [52]Department of Psychiatry, Hanyang University College of Medicine, Seoul, Republic of Korea. [53]Department of Neuropsychiatry, Hanyang University Hospital, Seoul, Republic of Korea. [54]Institute of Human Behavioral Medicine, SNU-MRC, Seoul, Republic of Korea. [55]Department of Child and Adolescent Psychiatry and Psychology, Hospital Clínic, Barcelona, Institut d'Investigacions August Pi i Sunyer (IDIBAPS), Barcelona, Spain. [56]Department of Medicine, University of Barcelona, Barcelona, Spain. [57]SAMRC Unit on Risk & Resilience in Mental Disorders, Department of Psychiatry, Stellenbosch University, Stellenbosch, South Africa. [58]GGZ inGeest Mental Health Care, Amsterdam, The Netherlands. [59]Department of Radiology, Bellvitge University Hospital, Barcelona, Spain. [60]Centre for Psychiatry Research, Department of Clinical Neuroscience, Karolinska Institutet & Stockholm Health Care Services, Region Stockholm, Stockholm, Sweden. [61]Department of Clinical Sciences, Lund University, Lund, Sweden. [62]Anxiety Treatment and Research Clinic, Department of Psychiatry and Behavioral Neuroscience, McMaster University, Hamilton, Ontario, Canada. [63]Department of Psychiatry and Behavioral Neuroscience, McMaster University, Hamilton, Ontario, Canada. [64]Department of Neuropsychiatry, Graduate School of Medical Sciences, Kyushu University, Fukuoka, Japan. [65]Monash Health & Department of Psychiatry, School of Clinical Sciences, Monash University, Melbourne, VIC, Australia. [66]Division of Child and Adolescent Psychiatry, Jane & Terry Semel Institute for Neurosciences, University of California, Los Angeles, CA, USA. [67]UCLA Brain Research Institute, Los Angeles, CA, USA. [68]Department of Psychiatry, University of Pittsburgh, Pittsburgh, PA, USA. [69]Departamento de Psicología Básica, Clínica y Psicobiología, Universitat Jaume I, Castellón de la Plana, Spain. [70]Department of Neuroscience, Yale University, New Haven, CT, USA. [71]Department of Experimental Psychology, Utrecht University, Utrecht, The Netherlands. [72]ATR Brain Information Communication Research Laboratory Group, Kyoto, Japan. [73]XNef, Inc, Kyoto, Japan. [74]Department of Psychiatry and Mental Health, University of Cape Town, and Neuroscience Institute, University of Cape Town, Cape Town, South Africa. [75]Department of Integrative Medicine, National Institute of Mental Health and Neurosciences (NIMHANS), Bangalore, India. [76]Pediatric OCD Consultation Service, Anxiety Treatment and Research Clinic, St. Joseph's Healthcare, Hamilton, Ontario, Canada. [77]Neuroscience Institute, New York University Grossman School of Medicine, New York, NY, USA. [78]Levvel, Academic Center for Child and Adolescent Psychiatry and Specialized Youth Care, Amsterdam, The Netherlands. [79]Imaging Genetics Center, Stevens Institute for Neuroimaging & Informatics, Keck School of Medicine, University of Southern California, Marina del Rey, CA, USA. [80]Department of Clinical Psychology, Shanghai Mental Health Center, Shanghai Jiao Tong University School of Medicine, Shanghai, P.R. China. [81]Department of Genetics and Genomic Sciences, Icahn School of Medicine at Mount Sinai, New York, NY, USA. [82]Charles Bronfman Institute for Personalized Medicine, Icahn School of Medicine at Mount Sinai, New York, NY, USA. [83]Department of Medical Physiology and Biophysics, Instituto de Biomedicina de Sevilla (IBiS), HUVR/CSIC/Universidad de Sevilla/CIBERSAM, ISCIII, 41013 Sevilla, Spain. [84]Department of Psychiatry, University of Cambridge, Herchel Smith Bldg, Robinson Way, Cambridge CB2 0SZ, UK. [85]SAMRC Unit on Risk & Resilience in Mental Disorders, Department of Psychiatry and Neuroscience Institute, University of Cape Town, Cape Town, South Africa. [86]Division of Human Genetics, School of Medicine, The University of Texas Rio Grande Valley, Brownsville, TX, USA. [87]Department of Psychology, Yale University, New Haven, CT, USA. [88]Center for Brain and Mind Health, Yale University School of Medicine, New Haven, CT, USA. [89]Wu-Tsai Institute, Yale University, New Haven, CT, USA. [90]Rutgers University, Robert Wood Johnson Medical School, New Brunswick, NJ, USA. [98]These authors contributed equally: Christopher Pittenger, Carolina Cappi. *A list of authors and their affiliations appears at the end of the paper. ✉e-mail: leonardo.saraiva@yale.edu; christopher.pittenger@yale.edu; carolina.cappi@rutgers.edu

ENIGMA-OCD Working Group

Leonardo Cardoso Saraiva[1,2]✉, João R. Sato[3], Isaac Sebenius[4], Nadza Dzinalija[5,6], Carla del Río-Torné[7,8], Fábio Godinho[9], Antonio C. Lopes[2], Thomas V. Fernandez[10], Monicke O. Lima[2], Vanessa R. Ramos[2], Ricardo Iglesio[9], Yoshinari Abe[11,12], Pino Alonso[7,8,13], Stephanie H. Ameis[14,15], Alan Anticevic[16], Ana Araújo[17,18], Paul D. Arnold[19,20], Srinivas Balachander[21], Nerisa Banaj[22], Marcelo C. Batistuzzo[2,23], Francesco Benedetti[24,25], Sara Bertolín[7,8,13], Irene Bollettini[25], Beatrice Bravi[25], Brian Brennan[26,27], Jan Buitelaar[28,29], João Castelhano[17,91], Miguel Castelo-Branco[17,18], Tiago F. T. Cerqueira[92], Sunah Choi[30], Patrícia Coelho[31,32], Beatriz Couto[31,32], Ana D. Costa[31,32], Sara Dallaspezia[25], Damiaan Denys[33,34], Isabel C. Duarte[17,35], Marco A. N. Echevarria[2], Goi Khia Eng[36,37], Afonso Fernandes[31,32], Sónia Ferreira[31,32], Jamie D. Feusner[38,39,40], Martijn Figee[41], Sophie M. D. D. Fitzsimmons[5,6], Leonardo F. Fontenelle[42,43,44], Rachael Grazioplene[1], Minji Ha[30], Alejandro Hinojosa[45], Marcelo Q. Hoexter[2], Chaim Huijser[46,47], Hao Hu[48], Anthony James[49], Jonathan Ipser[74], Minah Kim[50,51], Taekwan Kim[93,94], Jun Soo Kwon[52,53,54], Luisa Lazaro[13,55,56], Wieke van Leeuwen[33,34,95], Christine Lochner[57], Mafalda Machado-Sousa[31,32], Hein van Marle[33,34,58], Ignacio Martínez-Zalacaín[7,59], David Mataix-Cols[60,61],

Maria A. S. de Mathis[2], Elisa Melloni[25], José M. Menchón[7,8,13], Luciano Minuzzi[62,63], Pedro Moreira[32,96], Pedro Morgado[31,32], Emma Muñoz-Moreno[45], Astrid Morer[13,55,56], Laurens van de Mortel[33,34], Takashi Nakamae[11], Tomohiro Nakao[64], Janardhanan C. Narayanaswamy[21,65], Jin Narumoto[11], Erika L. Nurmi[66], Joseph O'Neill[66,67], Harin Oh[30], Ana E. Ortiz[55], Inkyung Park[30], Mary L. Phillips[68], John C. Piacentini[66], Maria Picó-Pérez[31,69], Fabrizio Piras[22], Federica Piras[22], Sara Poletti[25], Tjardo S. Postma[5,6], Chiang-shan R. Li[1,70], Eva Real[7,13], Janardhan Y. C. Reddy[21], Daan van Rooij[28,71], Yuki Sakai[11,72,73], Juliana B. de Salles Andrade[42], Freda Scheffler[74], Cinto Segalàs[7,8,13], Venkataram Shivakumar[75], Noam Soreni[63,76], Nuno Sousa[31,32], Emily R. Stern[36,37,77], Anouk van der Straten[33,34,78], Jinsong Tang[97], Sophia I. Thomopoulos[79], Hirofumi Tomiyama[64], Fernanda Tovar-Moll[42], Daniela Vecchio[22], Dick J. Veltman[5,6], Ganesan Venkatasubramanian[21], Chris Vriend[5,6], Zhen Wang[80], Anri Watanabe[11], Ysbrand D. van der Werf[5,6], Guido van Wingen[33,34], Kei Yamada[11], Qing Zhao[80], Alexander W. Charney[41,81,82], Youngsun T. Cho[1,10], Roseli G. Shavitt[2], Helen Pushkarskaya[1], Carles Soriano-Mas[7,8,13], Rafael Romero-Garcia[83,84], Paul M. Thompson[79], Dan J. Stein[85], Odile A. van den Heuvel[5,6], Anderson M. Winkler[1,86], Euripedes C. Miguel Filho[2], Christopher Pittenger[1,10,70,87,88,89] & Carolina Cappi[90,98] ✉

[91]LASI — Intelligent Systems Associate Laboratory, Guimarães, Portugal. [92]CFisUC, Department of Physics, University of Coimbra, Coimbra, Portugal. [93]Department of Bio and Brain Engineering, Korea Advanced Institute of Science and Technology, Daejeon, Republic of Korea. [94]Mental Health Neuroscience Department, Division of Psychiatry and Max Planck UCL Centre for Computational Psychiatry and Ageing Research, Queen Square Institute of Neurology, UCL, London, UK. [95]Arkin Mental Health Care, Department of Psychiatry, Amsterdam, The Netherlands. [96]School of Psychology, University of Minho, Braga, Portugal. [97]Department of Psychiatry, Zhejiang University School of Medicine, Hangzhou, China.